EUROPEAN ORGANIZATION FOR NUCLEAR RESEARCH

Engineering Department (MME-MM)

CRACOW UNIVERSITY OF TECHNOLOGY

Faculty of Mechanical Engineering

MASTER OF SCIENCE THESIS

Dawid Jarosław Marcinek

EXPERIMENTAL STUDY OF DISCONTINUOUS PLASTIC FLOW, PHASE TRANSFORMATION AND MICRO-DAMAGE EVOLUTION IN DUCTILE MATERIALS AT CRYOGENIC TEMPERATURES

CERN supervisor:

Dr. **Stefano Sgobba**

University supervisor:

Prof. **Błażej Skoczeń**

Cracow, 2009

Acknowledgement

I would like to express my gratitude to my University supervisor, Professor Błażej Skoczeń, for his help and guidance throughout this Thesis and the idea of spending the training period at the European Organization for Nuclear Research (CERN), where the experimental part of this work has been carried out.

I am also very thankful to my CERN supervisor, Doctor Stefano Sgobba, for giving me the opportunity to carry out the above mentioned training and for all his support during my stay at CERN.

Finally, I would like to thank all members of the EN-MME-MM group, who hosted me at CERN, especially Alexandre Gerardin and Markus Aicheler, for their everyday help and hospitality.

Contents

Przedmowa w języku polskim

/Foreword in Polish/

Niniejsza praca magisterska pt. "Badania doświadczalne nieciągłego płynięcia plastycznego, przemiany fazowej oraz ewolucji mikro-uszkodzeń w materiałach plastycznych stosowanych w temperaturach kriogenicznych" przedstawia szczegółowo procesy występujące podczas rozciągania materiałów w niskich temperaturach. Zawarte tu zostały wyniki badań eksperymentalnych wykonanych, w laboratorium Europejskiej Organizacji Badań Jądrowych (CERN), pod kątem lepszego poznania zjawisk: nieciągłego płynięcia plastycznego, przemian fazowych i ewolucji mikro-uszkodzeń. Ponadto, praca zawiera dokładny opis sprzętu laboratoryjnego użytego do przeprowadzenia eksperymentów niskotemperaturowych oraz przybliża matematyczną interpretację w/w zjawisk niezbędną dla prawidłowego projektowania konstrukcji pracujących w temperaturach kriogenicznych.

Pierwszy rozdział nakreśla obraz ośrodka naukowego CERN wraz z jego kluczowym eksperymentem Wielkiego Zderzacza Hadronów (LHC) działającym w temperaturze bliskiej absolutnego zera. Następnie omówiona jest historia badań zjawisk niskotemperaturowych zwracając uwagę na najistotniejsze osiągnięcia w tej dziedzinie oraz ich praktyczne zastosowania.

Rozdział drugi wprowadza ogólne zrozumienie zjawisk, występujących podczas rozciągania materiałów plastycznych w niskich temperaturach, będących przedmiotem tej pracy dyplomowej tj.: nieciągłego płynięcia plastycznego, przemian fazowych i ewolucji mikro-uszkodzeń.

Kolejny rozdział szczegółowo opisuje wyjątkowy zestaw sprzętu laboratoryjnego zaprojektowany w CERN'ie do prowadzenia testów rozciągania materiałów w ciekłym helu. Zaczynając od maszyny wytrzymałościowej opis ten obejmuje kriostat z elementami składowymi, dokładne dane czujników użytych do pomiarów (wraz z niektórymi certyfikatami kalibracji w załącznikach) oraz system rejestrujący dane eksperymentalne.

W czwartym rozdziale zawarte zostały, w postaci wykresów z krótkim opisem, wyniki testów rozciągania materiałów stosowanych w systemach kriogenicznych. Główna uwaga została zwrócona w kierunku czystej miedzi, niemniej nie brakuję przykładów stopów miedzi z cyrkonem oraz stali nierdzewnej. Zamieszczone wykresy obrazują zjawisko nieciągłego płynięcia plastycznego w ujęciu makroskopowym na przestrzeni całego testu oraz w ujęciu mikroskopowym dla precyzyjnie zarejestrowanych pojedynczych „skoków”.

Piąty rozdział jest skoncentrowany na kinetyce badanych procesów niskotemperaturowych. Została tu podjęta próba identyfikacji parametrów i praw kinetyki trzech rozpatrywanych zjawisk kriogenicznych.

Podsumowując podkreślona jest niezwykłość opisanych tu badań ze względu na precyzję osiągniętych wyników. Przy współcześnie niskim poziomie wiedzy na temat omawianych tu zjawisk praca ta stanowi interesującą pozycję pośród literatury o tematyce eksperymentalnej.

Chapter 1

Introduction

1.1 About CERN

The European Organization for Nuclear Research, known as CERN[1] is one of the world's largest and most respected centres for scientific research [1]. Situated near Geneva on the Franco-Swiss border, CERN has been founded in 1954. The Organization counts twenty European member states, six states having observer status and many more who are involved in the international collaboration on numerous experiments (Fig. 1.1).

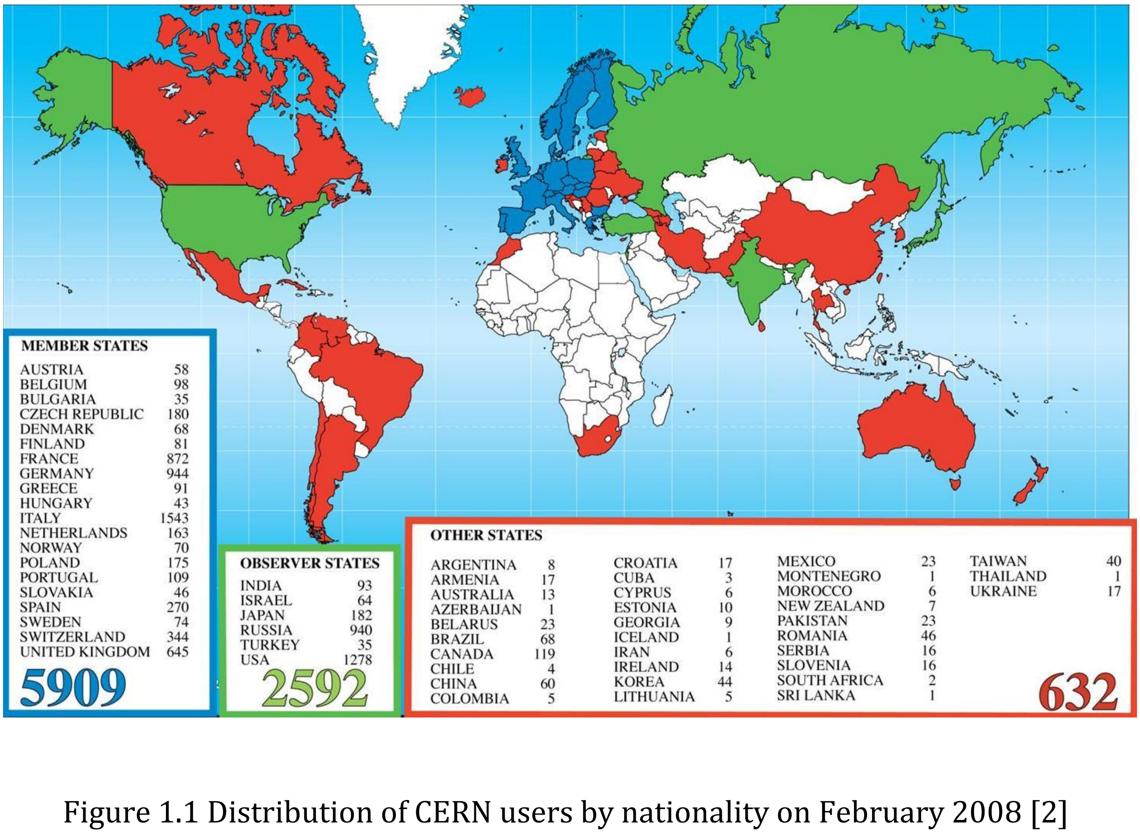

Figure 1.1 Distribution of CERN users by nationality on February 2008 [2]

[1] fr. **C**onseil **E**uropéen pour la **R**echerche **N**ucléaire

The main focus of CERN is directed towards discovering basic constituents of matter by providing the international scientific community with particle accelerators and other instruments needed for research in high-energy physics (Fig. 1.2). The particle beams are boosted in the accelerators to high energies and collided with each other or with stationary targets. The results of these collisions are recorded by the so-called detectors. The scientists use these observations to answer questions related to the origin of Universe.

In 2008/2009 the largest and most powerful particle accelerator in the word – the LHC[2] has been completed. Basically, it is an underground ring of 27 km in circumference equipped with long superconducting magnets and suitable accelerating structure to boost the energy of heavy particles.

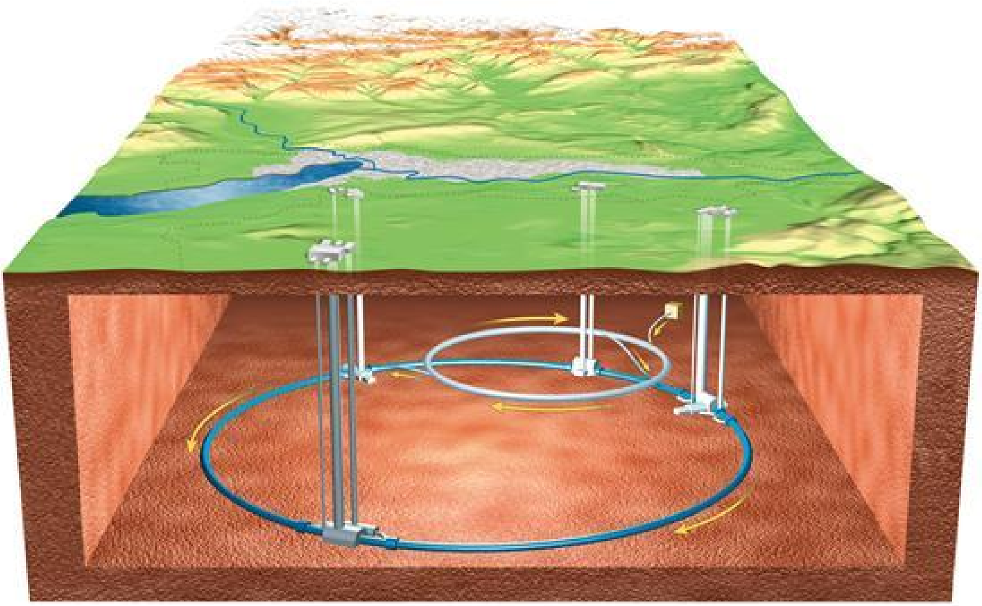

Figure 1.2 Drawing of the CERN underground particle accelerator LHC [2]

CERN has been divided into eight departments, each of them having its own profile:

- PH – Physics
- BE – Beams
- EN – Engineering
- FP - Finance and Procurement
- IT - Information Technology
- TE - Technology
- HR - Human Resources
- GS - General Infrastructure Services

[2] **L**arge **H**adron **C**ollider

1.2 The LHC cryogenic system

The LHC cryogenic system is the largest system of such kind in the world and in the same time one of the coldest places on Earth [3]. It has to supply some 150 kW power to refrigerators at 4.5 K and some 20 kW to these working at 1.9 K to maintain the LHC ring (4700 tonnes of material in each of the eight sectors) at the temperature of super-fluid helium 1.9 K (-271.3 °C). Such temperature – in the proximity of absolute zero - is required for the magnets to operate safely in the regime of superconductivity (Fig. 1.3).

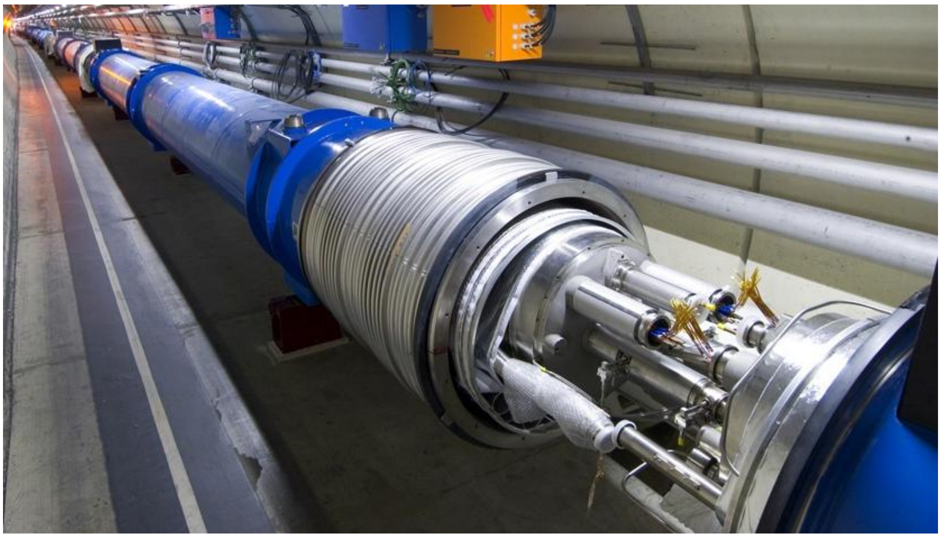

Figure 1.3 Underground portion of the LHC ring [2]

Five ‘cryogenic islands’ form basis of the refrigeration system. Each of them distributes the coolant and carries over a long distance many kilowatts of refrigeration. The cooling process takes a couple of weeks and uses about 10000 t of liquid nitrogen and 120 t of liquid helium. It is carried out within three main phases:

- cool down to 4.5 K (-268.7ºC);
- filling with liquid helium the cold mass;
- final cool down to 1.9 K (-271.3ºC).

About 90 t of liquid helium is used in the magnets and some 30 t in the pipes and refrigerator units.

1.3 Experimental research carried out at low temperatures

The beginning of cryogenic research (by IIR[3]: the technology and science of temperatures below 120 K) goes back to 19th century [4]:

- in 1877 Cailletet and Pictet performed first liquefaction of air,
- in 1883 Olszewski and Wroblewski separated oxygen and nitrogen,
- in 1898 Dewar carried out first liquefaction of hydrogen thanks to his invention of the vacuum-insulated, radiation-shielded container.

Next and very important step of low temperature research was liquefaction of helium performed in 1908 by Kamerlingh Onnes, which led to discovery of such phenomena like superconductivity (1911, by Kamerlingh Onnes) and superfluidity (1928, by Keeson). These phenomena remain still today major areas of research.

Nowadays, as a result of sustained development of cryogenics towards the temperatures close to absolute zero, the specialized laboratories can attain values down to about 0.1 nK. Thanks to development of the so-called type II superconductors and the refrigeration technology down to the temperature of He II, the superconductivity and the superfluidity became industrial techniques implemented in a large scale instruments:

- nuclear magnetic resonance systems,
- magnetic-confinement fusion devices (Fig. 1.4),
- high-energy particle accelerators (see chapter 1.2).

When implementing low temperature science to practical technologies, the problems so far unknown have appeared. The phenomena of serrated yielding, plastic strain induced γ-α’ phase transformation and evolution of micro-damage became one of the most interesting scientific matters currently under investigation.

---

[3] **I**nternational **I**nstitute of **R**efrigeration

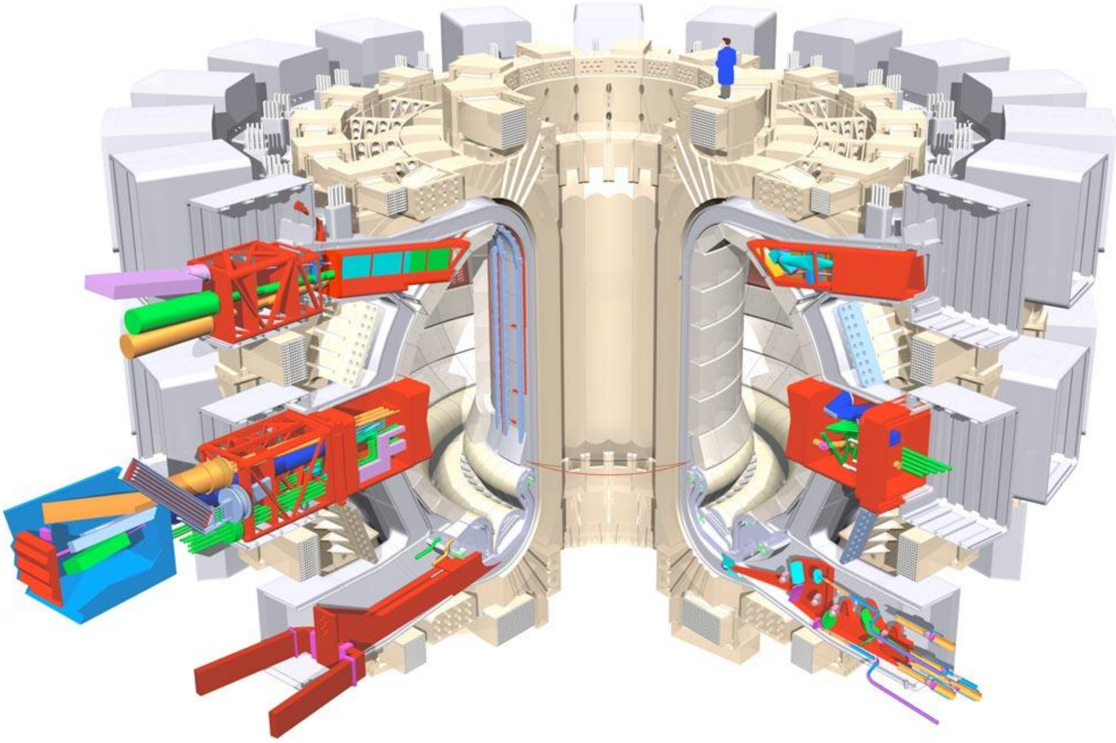

Figure 1.4 Project ITER[4] - overview of large fusion tokamak

One of the first papers on the instability of plastic flow of metals at low temperatures was published by Basiński [5] in 1957. Since then, a number of researchers tried to find explanation of these phenomena. Basically, three possible reasons for plastic flow instabilities have been suggested by Dolgin and Natsik [6]:

- thermo-mechanical (thermally activated), first described by Basiński [5, 7] and later discussed based on computer simulation by Shibata [8],
- dislocation-dynamical (athermal), first described by Seeger [9],
- geometrical, described by Trefilov, Milman and Firstov [10].

Over a span of years many papers were published on the above-mentioned cryogenic phenomena, referring to experimental studies, but only some of them described the experiments carried out at very low temperatures [11 – 20].

---

[4] **I**nternational **T**hermonuclear **E**xperimental **R**eactor

1.4 The aim of the Thesis

The present Thesis deals with three low temperature phenomena occurring in ductile materials subjected to mechanical loads: serrated yielding, plastic strain induced γ-α' phase transformation and evolution of micro-damage:

- the Thesis explains the physical mechanisms governing each phenomenon at the micro and macroscopic levels;
- the document describes in detail the advanced laboratory equipment needed for cryogenic experiments;
- the results of tests carried out with unique precision and focused on serrated yielding and evolution of micro-damage (the observations were made with different strain rates and with the use of different materials) are presented;
- validation of suitable kinetic laws and identification of parameters for tested materials is carried out.

Chapter 2

Phenomena occurring in ductile materials at cryogenic temperatures

2.1 Discontinuous plastic flow

Serrated yielding is a low temperature phenomenon which can be observed as abrupt load drops on tensile stress-strain curve in many different materials. It is manifested by sudden "jumps" of stresses as a function of strain (time) followed by load drops and temperature oscillations (Fig. 2.1). On the macroscopic scale it is similar to PLC[5] effect which occurs in some materials (for example iron) at higher temperatures. In the cryogenic conditions (close to absolute zero) the specific heat, the thermal conductivity and the thermal expansion coefficient tend to zero. The heat transport is based mainly on acoustic phonons propagation and on the Fermi gas (electrons).

Estrin and Tangri [21] suggested some elements of mathematical model of the temperature dependence of the flow stress. According to the theory of thermal instability serrated yielding appears due to the heat generation during plastic deformation. Consideration of homogenous temperature distribution throughout the cross-section of a specimen was possible under a specific condition of correlation between the specimen size and the heat exchange with thermal bath. The heat transfer coefficient must comply with the equation:

$$hR/2K \ll 1 \tag{2.1}$$

---

[5] **P**ortevin-**L**e **C**hatelier

where h is the surface heat transfer coefficient, R is the specimen radius, and K is the heat conductivity of the specimen.

Dolgin and Natsik [6] created a temperature - strain rate diagram of jump-like deformation in a Copper-aluminium alloy with the area of serration (Fig. 2.2). Here the phenomenon is limited by the lower and the upper strain rates as a function of temperature. According to this point of view serrated yielding can be observed in pure Copper only below some critical temperature of $T_{cr} \leq 10$ K and strain rate of $d\varepsilon/dt > 10^{-5} \div 10^{-3}$ s^{-1} .

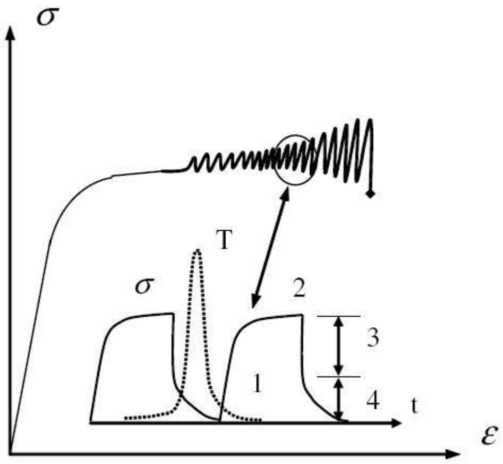

Figure 2.1 Illustration of serrated yielding with four stages of the process [37]

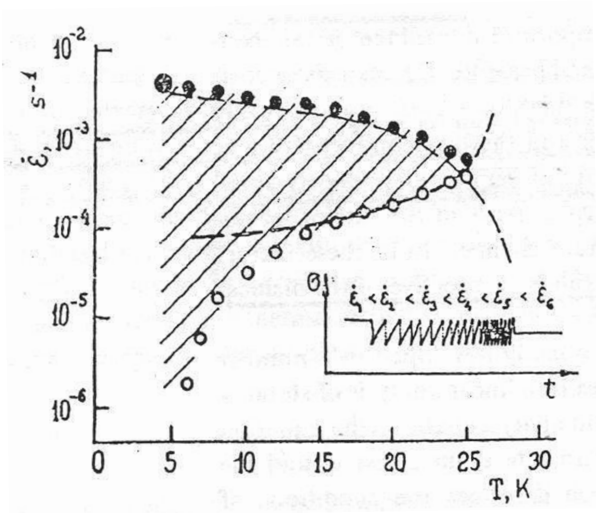

Figure 2.2 Strain rate - temperature diagram of serration in Copper-aluminium alloy [6]

Strong temperature dependence of serrated yielding was also pointed out by Obst and Nyilas [15] as a factor of different kinds of dislocations motion. It is shown that during strain hardening dislocation pile-ups are created at strong obstacles. At low temperature edge dislocations have predominant character and when the temperature threshold (specific for different materials) is reached screw dislocations start to have predominant character. Then, correspondence between the temperature and the plastic flow instability can be seen.

2.2 Plastic strain induced γ-α' phase transformation

The phenomenon of diffusionless phase transformation occurs in metastable materials at cryogenic temperatures. As a result of low temperature plastic flow, the crystal lattice transforms from the paramagnetic FCC[6] austenitic phase γ into ferromagnetic BCC[7] martensitic phase α' that is characterized by more brittle behaviour. This kind of diffusionless phase transformation is commonly known for TRIP[8] austenitic steels. At the temperatures in the proximity of absolute zero phase transformation generated by plastic deformation proceeds at high speed and in some cases can lead to almost complete replacement of γ phase by the brittle α' phase.

During deformation of metastable stainless steels (among other: grades 304, 304L, 316L) at cryogenic temperatures a hardening behaviour can be observed [22]. It is a reaction to production of the plastic strain induced martensite which significantly influences the mechanical properties of the alloys (Fig. 2.3).

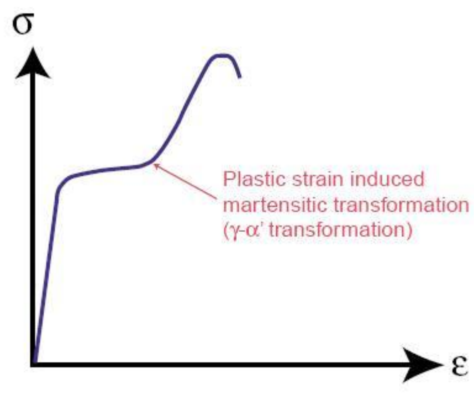

Figure 2.3 Stainless steel influenced by phase transformation at low temperatures [22]

---

[6] **F**ace-**C**entred-**C**ubic
[7] **B**ody-**C**entred-**C**ubic
[8] **TR**ansformation **I**nduced **P**lasticity

The FCC-BCC phase transformation can be induced not only by low temperature deformation but also by high magnetic field as described by Morris, Chan and Mei [23]. On the other hand, Suzuki, Fukakura and Kashiwaya pointed out two main phenomena associated with FCC-BCC phase transformation in stainless steels [24]:

- spontaneous transformation while cooling down. For the temperature called Neel's temperature the martensite rate reaches a maximum.
- strain induced transformation related to plastic strain at cryogenic temperatures. It can be classified as a dissipative process of the strain induced martensitic transformation (irreversible).

Magnetic permeability of the sample is assumed to be a good mean of detection of martensite presence. It is because the intensity of the local plastic strain fields is directly linked to the amount of α' martensite which exhibits a ferromagnetic behaviour.

2.3 Evolution of micro-damage

The phenomenon of formation and propagation of the micro-damage fields (micro-cracks and micro-voids) occurs due to inelastic strain fields at cryogenic temperatures accompanied by high yield and tensile strength. It is an irreversible and dissipative process which leads to "softening" of the material. This phenomenon is of great importance for materials used at the temperatures close to absolute zero. The source of micro-damage fields in two-phase materials is related either to inclusions or to the matrix. Inclusions of type α' are often carriers of the so-called short cracks. They can start propagating inside the inclusion and next spread to the surrounding matrix.

Martensite inclusions and micro-defects coexist in the same volume of material [25]. Damage is represented by a surface density of micro-cracks and micro-voids reflected by the scalar damage variable. Thus, damage parameter is defined as:

$$D = \frac{dS_D}{dS} \quad ; \quad 0 \le D \le 1 \tag{2.2}$$

where dS_D stands for the surface of intersection of the micro-defects with a given plane within the RVE[9] and dS is the total cross-section surface (Fig. 2.4).

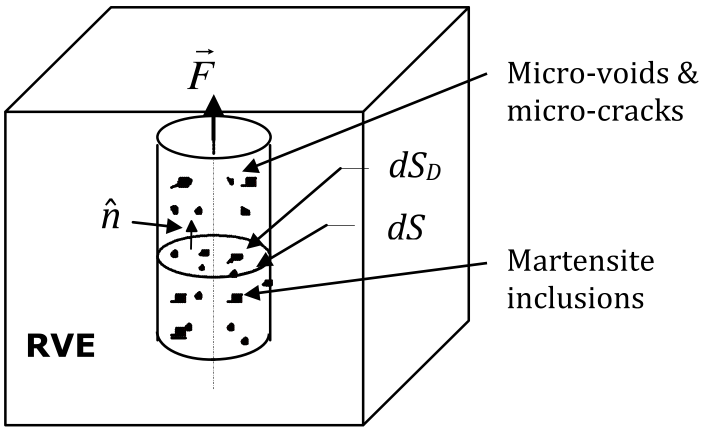

Figure 2.4 RVE with martensite inclusions and micro-damage [25]

Measurements of the evolution of elasticity modulus offer a possibility to detect the intensity of ductile damage. Due to quite similar elastic properties of the martensite and the austenite, it is assumed that the martensitic transformation does not modify the elastic properties of the two-phase material. Evolution of the damage parameter D can be identified by suitable measurements of the current elasticity modulus E (along the unloading paths):

$$\tilde{E} = E(1 - D) \tag{2.3}$$

Thus, in order to determine the evolution of damage associated with the accumulated plastic strain it is sufficient to run a simple tensile test with several unloadings.

[9] **R**epresentative **V**olume **E**lement

Chapter 3

Experimental set-up for testing materials applied at low temperatures

3.1 Tensile testing machine

The low temperature tensile tests were carried out using high efficient cryogenic testing system developed in EN-MME-MM[10] at CERN. The cryostat which holds tested specimen and most of data acquisition sensors (with the exception of external load cell) were filled/immersed with/in liquid helium (4.2 K) and mounted in the tensile testing machine (Fig. 3.1).

Figure 3.1 Tensile test machine [26]

[10] **En**gineering Department **- M**echanical & **M**aterials **E**ngineering **- M**etallurgy & **M**etrology

The data coming from the sensors were transferred through a signal conditioner to a PC equipped with data acquisition PCI card. The visualization and the storage of test data, as well as the calculation of the characteristics of material were carried out by a program developed under LabView.

For testing the electro-mechanical screw-driven 200 kN UTS tensile machine with precision of 1 μm stroke displacement was used. The machine was controlled by a PC connected with Dion Pro software. The stroke speed was determined by the strain rate range of serrated yielding which is approximately between $5*10^{-4}$ s^{-1} and $5*10^{-3}$ s^{-1}. When the gauged length of sample was equal to 25 mm then the stroke speed varied between 0.0125 mm/s and 0.125 mm/s.

3.2 Cryostat structure

For tests at low temperatures the quality of the cryostat was very fundamental [27]. For this reason the CERN developed its own cryostat. The overall drawing of the cryostat is presented in Figure 3.2. This cryostat is composed of two parts:

- female part composed of a traditional Dewar comprising a double partition and a super insulator;

- male part which supports the specimen. It consists of the stem of traction, head, glass fibre columns, element fixing the specimen, mobile screen and the cryostat as shown in Fig. 3.3. With an aim of reducing the risk of buckling of the glass fibre columns, a stabilizer was fixed on the three columns. It reduces the effective length by half. Three mobile copper screens ensure good heat transfer between evaporated gas, the stem of traction and the wall of the tank. They make it possible to decrease the losses by conduction. Electric connections of the sensors and three accesses for: the helium supply, the stem of traction and the helium recovery were combined in the head of the cryostat.

The cryostat is placed in the tensile testing machine by means of fixings. The force on the specimen is transmitted via the needle stem of traction. It supports a maximum force of 15 kN with the helium consumption of approximately 5 L for an endurance of one hour test.

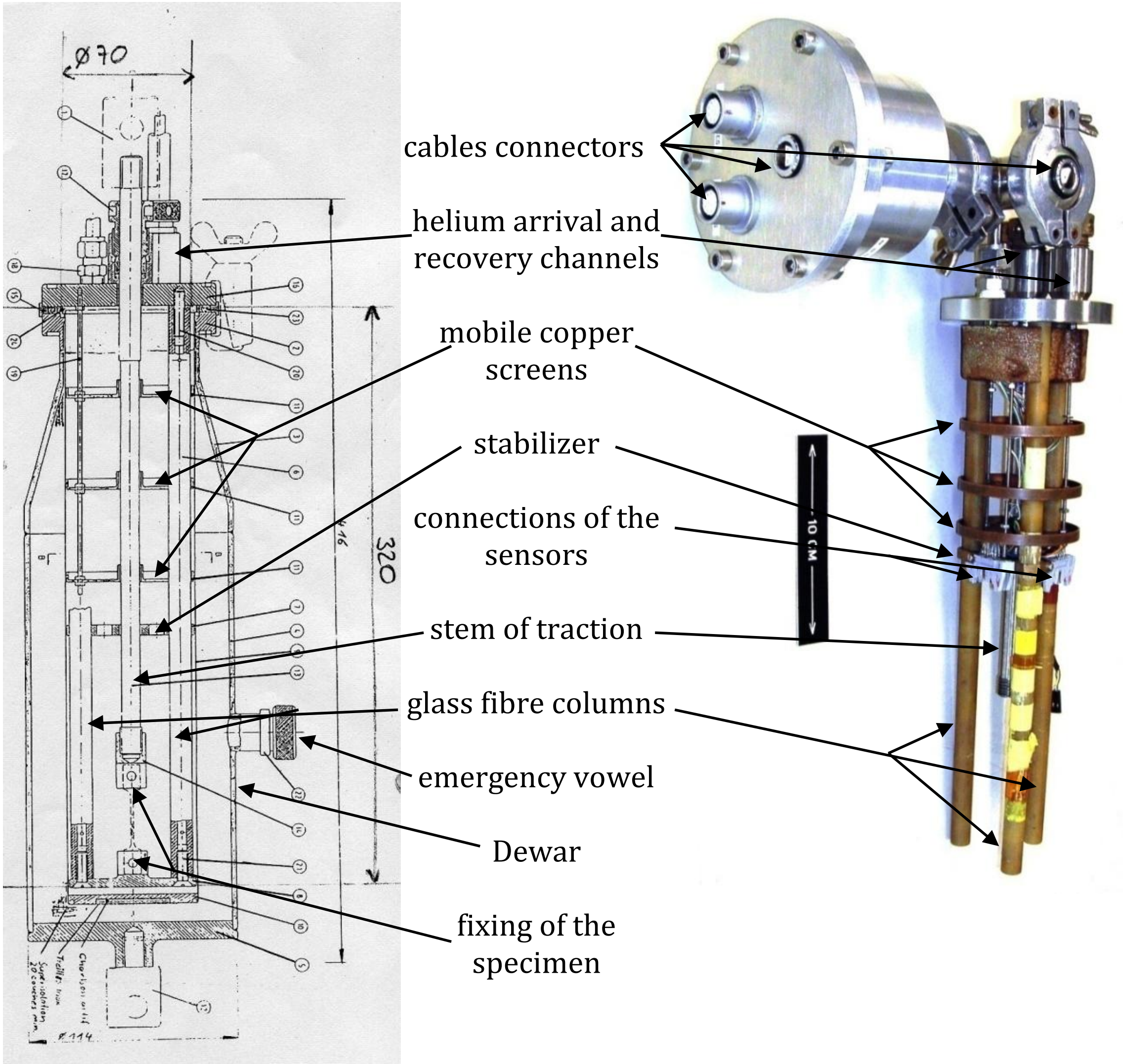

Figure 3.2 Cryostat drawing [28]

Figure 3.3 Male part of cryostat

Limited space between glass fibre columns was used to construct data acquisition environment around tested specimen (Fig. 3.4).

Two resistances of the Allen Bradley type (characterized by strongly increasing resistance below temperature of 30 K), very sensitive to evolution of temperature were used with an aim of detecting the presence of helium on a minimum and a maximum level. These resistances were placed at 90 mm and 160 mm counting from the bottom of the tank. Thus, it was possible to ensure the immersion of the specimen in the liquid.

A simple resistance was also used to accelerate the evaporation of helium at the end of the test.

Two inductive sensors were assembled on an extensometer stretched (fixed) over the gauged length of the specimen. The average value of both signals emitted by these sensors made it possible to determine the deformation of the specimen in the elastic zone and in the beginning of the plastic range. A potentiometer equipped with carbon track was used to measure elongation of the specimen as soon as the range of the inductive sensors (3 mm) was exceeded and until the rupture.

An internal load cell was mounted between the sample and the stem of traction to provide high precision readout of tension force during the test.

A temperature sensor of small dimensions allowed the readout of temperature directly on the sample in the range where serrations were observed.

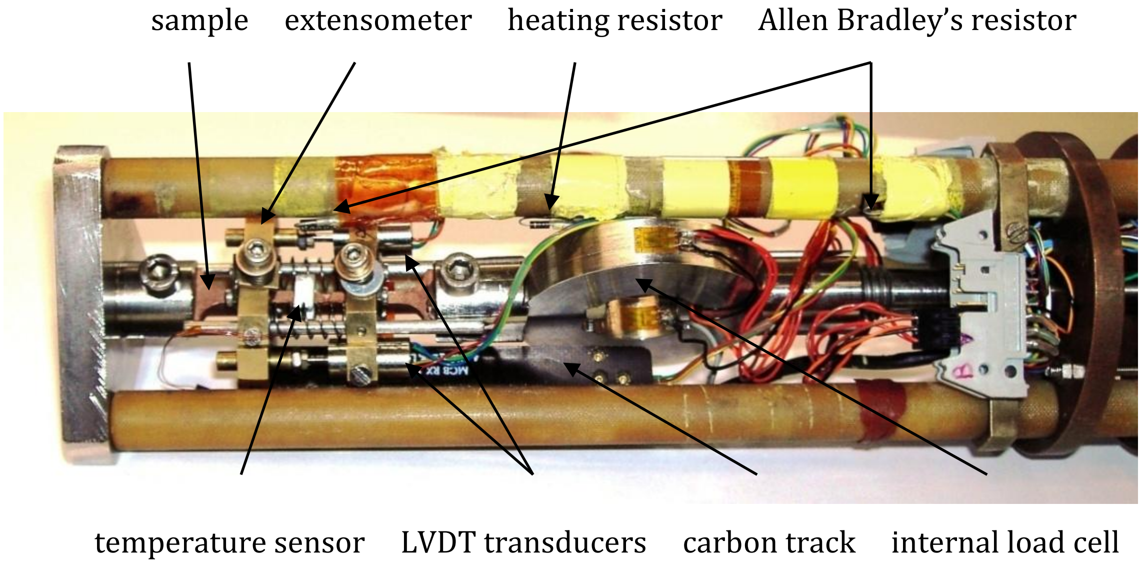

Figure 3.4 Installation of the sample and the sensors inside the cryostat

3.2.1 Extensometer

The sample size and the precision of measurements imposed the use of an extensometer which constituted a specific support for the sensors (Fig. 3.5). In order to carry out tensile tests on various samples the gauged length of which could vary from 2.5 mm to 25 mm and the section from 1 mm^2 to 9 mm^2, the extensometer had a modular concept. It consisted of an assembly of two elements. The lower part carried the cores of the inductive sensors and the body of the carbon potentiometer. The upper part supported the bodies of the inductive sensors as well as the cursors of the potentiometer. Each of these two units was rigidly fixed with respect to the other via two tightly polished columns equipped with screws. During the test, the extensometer slipped without jolts thanks to these two columns.

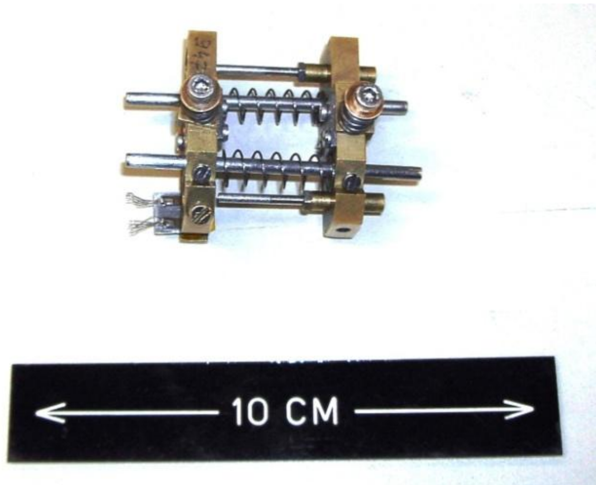

Figure 3.5 Extensometer

The sample was centred between two inductive sensors thanks to the guides with removable knives present on each frame of the extensometer. The contact between the extensometer and the specimen was ensured by knives. The force of fixing could be controlled with the screws and the springs installed behind the mobile knives. When the section of the specimen decreased during traction, these springs were expanded thus allowing to keep correct fixing of the sample. After having installed the sample, the extensometer formed only one rigid element which could be easily fixed in the cryostat, as shown in Figure 3.4.

3.2.2 Temperature sensor

The sensor used for temperature measurements was the resistive probe Cernox CX-1050-SD-30 of Lake Shore Cryotronics (Fig. 3.6). This sophisticated sensor has a resolution of 5 mK and a response time of 15 ms at 4.2 K. Its small dimensions (3.2 mm x 1.9 mm x 1 mm) and its weight of 30 mg was well adapted to the tests carried out in the cryostat (Fig. 3.7).

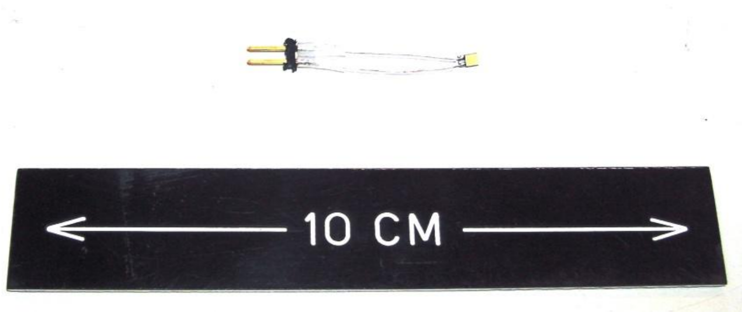

Figure 3.6 Temperature sensor

The chip was mounted on sapphire base with alumina body. Hermetic lid seal was performed by gold-tin solder. Two gold-plated copper leads were attached for connection purpose [29]. The interior of the case was vacuum tight. A hermetic but - titanium joint guaranteed the sealing (Fig. 3.8).

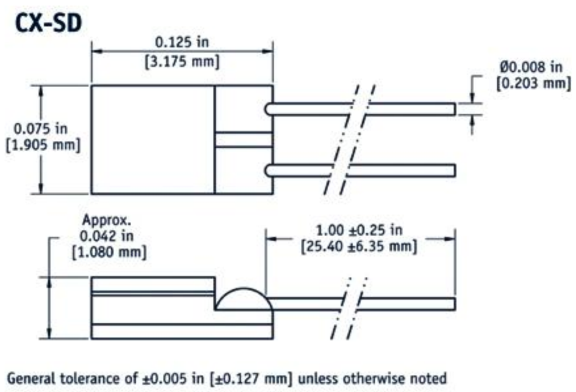

Figure 3.7 Sensor dimensions

Figure 3.8 Sensor structure

The sensor was powered by using a 10 mV voltage, provided by a conditioning set-up. This sensor was adapted by CERN for temperatures ranging from 1.6 K to 303 K. The nonlinear curve of resistance as a function of temperature was obtained by means of the Chebychev polynomial. The curve and the certificate of calibration as well as the equation of adjustment are presented in Appendix A.

3.2.3 LVDT transducer

The inductive sensors used for the tests were LVDT[11] Sensorex SX 9W3 (test and inspection data are presented in the Appendix B). LVDT transducers were intended for the applications in severe industrial environment: extreme temperatures or pressures, high accelerations and multiple cycles (Fig. 3.9).

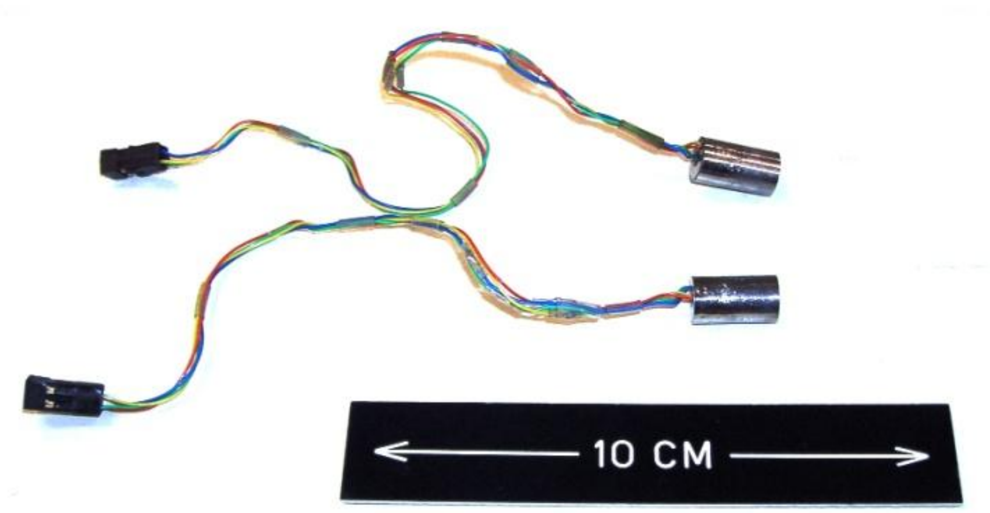

Figure 3.9 LVDT transducers

[11] **L**inear **V**ariable **D**ifferential **T**ransformer

This transformer device produces an electrical output proportional to the displacement of a free moving core [30]. This type of transducer consists of a primary coil powered by an AC signal and two secondary coils. When the core moves inside the coils, voltages V1 and V2 are induced in the secondary coils, and remain proportional to the displacement. Both secondary coils are connected in series and keep opposite polarities, so that the output signal is equal to the difference between these voltages. In this configuration, the output voltage is null when the core is in the centre. When it moves out from the centre, the differential voltage increases. The output voltage is then rectified in order to get a DC signal proportional to the displacement of the core (Fig. 3.10).

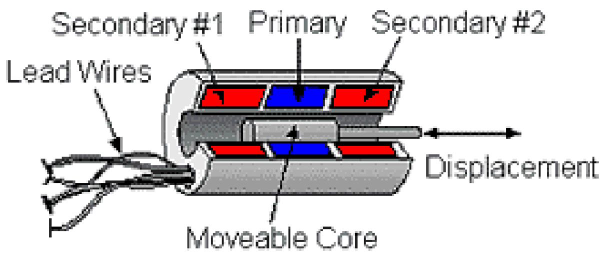

Figure 3.10 Internal structure of LVDT transducer [30]

The characteristic of the sensor is linear in the range of 0-3 mm and does not depend significantly on the temperature [27]. In order to obtain better precision, the sensors were calibrated at the temperature of the test thanks to the LabView program. The response time of the sensor was 2.5 ms; the resolution reached was about 1 μm out of ± 1.5 mm. Two sensors were placed on both sides of the specimen and calculation of the average of both signals made it possible to compensate for a possible asymmetry in the motion of the frame of the extensometer.

3.2.4 Carbon track

Beyond 3 mm of displacement, the inductive sensors relegate measurement to the MCB RX 13 50 carbon track (Fig. 3.11). This potentiometer has 50 mm range of displacement and it functions thanks to the RX 13 cursor. It has a read out of 0.1 mm resolution.

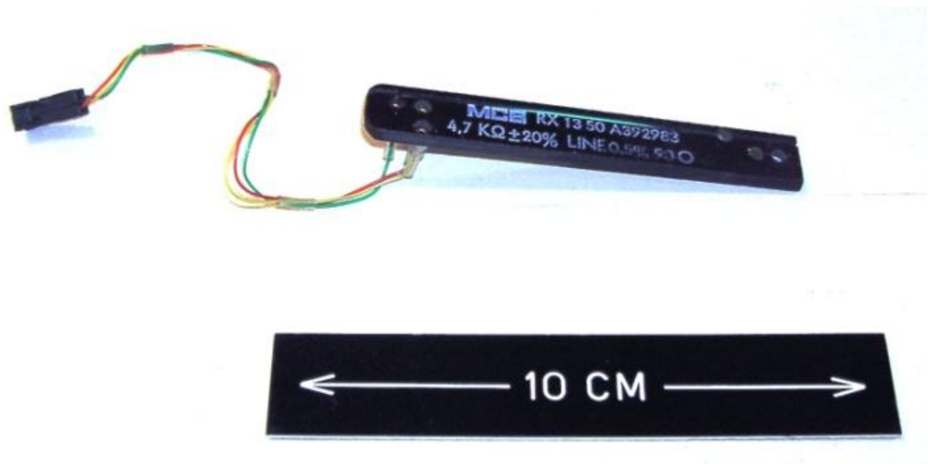

Figure 3.11 Carbon track

3.2.5 Internal load cell

The design of the internal load cell (made at CERN [26]) was accompanied by the following constraints:

- application at very low temperatures (down to absolute zero),
- geometry allowing to place the strain gauges in order to obtain a linear signal,
- limited space inside the cryostat,
- the fixings well adapted to the stem of traction and the geometry of the specimen.

Dimensions of the sensor were set to: 53 mm in diameter, 15 mm of thickness and 10 mm of width. The load-cell was equipped with two holes of 6 mm for the screws of fixing and the flat parts on the inner surface to add a nut. The flat parts brought back the minimum diameter to 13 mm (Fig. 3.12).

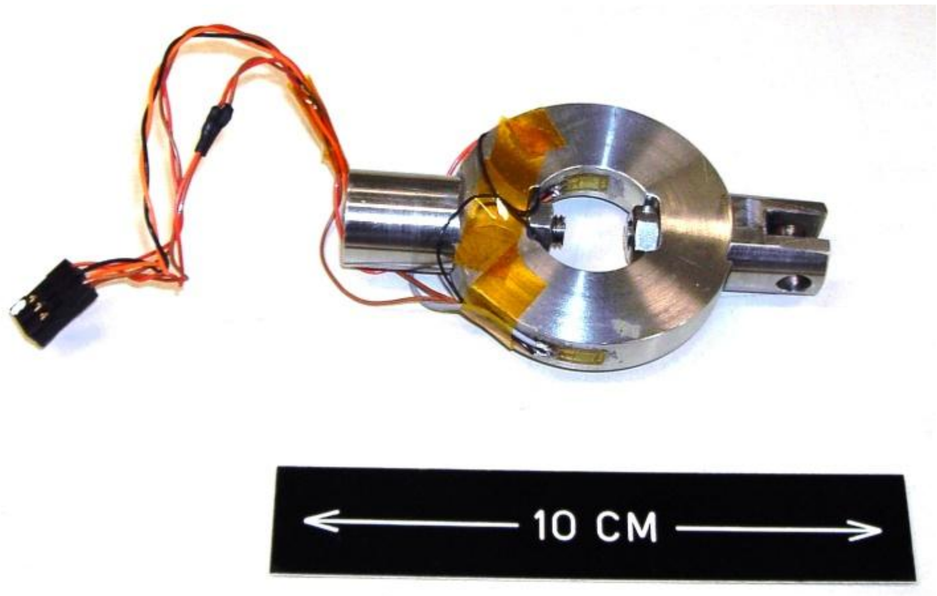

Figure 3.12 Internal load cell

The strain gauges 3/350LC11 VISHAY were the resistances fixed on the annular part of the sensor. The force applied along the traction axis induces corresponding deformation of the annular disc and, consequently, deformation of the strain gauges. The resistance of the gauges varies according to the formula:

$$\frac{\Delta R}{R} = k\frac{\Delta L}{L} \tag{3.1}$$

with k factor depending on the type of gauge. The gauges were integrated in the Wheatstone bridge and the imbalance voltage measured. Relation between this voltage and the force was obtained by suitable calibration. The maximum force supported by this load cell was of 4200 N.

3.2.6 External load cell

The external load cell Maywood U2000 was mounted between the traction machine and the cryostat stem of traction (Fig. 3.13). It can measure force up to 25 kN with the excitation level of 10 VDC and the resolution of 0.27 N. The output signal was strongly amplified.

The robust shear web design used four strain gauges connected to Wheatstone bridge, strategically placed to counteract and minimize errors due to unwanted side or non-axial forces [31]. Low deflection and high frequency response were beneficial in high speed measurements, especially where peak loads were being monitored (for certificate of calibration see the Appendix C).

Figure 3.13 External load cell [32]

3.2.7 Specimen

Flat samples used for the tests had the following dimensions: 60 mm in length, 3 mm of thickness, 3 mm of width along the gauge length and 13 mm of width along the heads (Fig. 3.14). Two heads on the specimen extremities allowed fixing it on the stem of traction. In order to measure the heating during serrations, a notch large enough to contain the sensor was machined in the centre of the specimen. The notch is shown in Figure 3.15. The reduction of section allowed on one hand to concentrate the strains in the groove and on the other hand to make sure that the temperature indicated by the sensor was well the temperature of the sample. The sensor maintained on the specimen during traction was fixed by specially dimensioned grip.

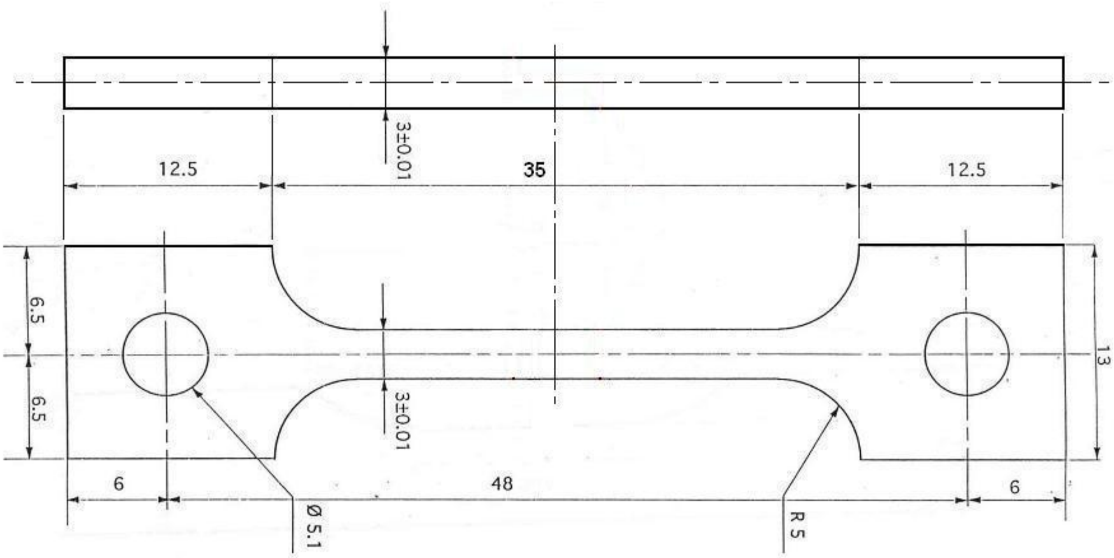

Figure 3.14 Specimen dimensions [33]

Figure 3.15 Samples with and without notch

The notch caused asymmetry of sample which implied bending during the test. This had an influence on all the microstructure processes taking place in the zone of interest. This matter became a background for modelling of samples in such a way to attain best data recording results by concentrated measurements in a well foreseen serrated yielding area.

3.3 Data acquisition system

3.3.1 Signal conditioner

A conditioning set-up has been defined for each sensor (Fig. 3.16). Two instruments were developed on-purpose at CERN: for the internal load cell (sensor of force) and for the temperature gauge [32].

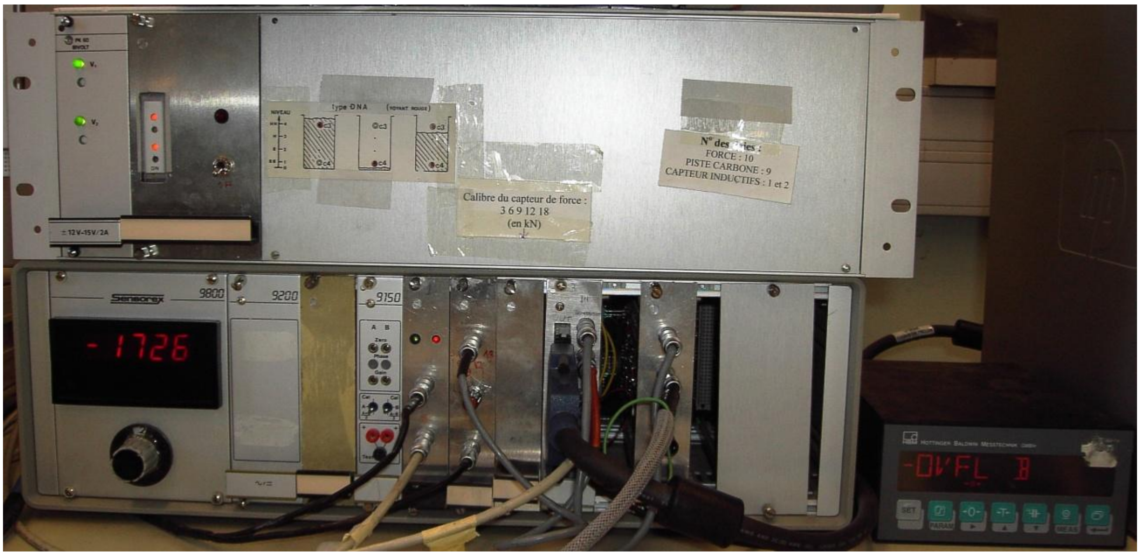

Figure 3.16 Signal conditioner

The function of the conditioning set-up for the sensor of force consists in definition of the amplification ratio of the output signal with a variable gain. The choice of suitable gain was carried out thanks to a rotary button with which one selected a gauge among: 3 kN, 6 kN, 9 kN, 12 kN and 18 kN.

The set-up for the temperature gauge provided a stabilized power supply at 10 μA and amplified the signal with a profit of 100. The signal was filtered to remove the background noise. The shielding of the cable, connecting the sensor to the set-up was connected to the mass. Thus, it was possible to avoid external perturbations.

3.3.2 PCI card

Data from the signal conditioner was further transferred and stored on a PC computer based on AMD Athlon processor technology and supplied with the NI[12] PCI-6036E card (Fig. 3.17). The DAQ[13] board was equipped with sixteen 16-bit analogue inputs and two 16-bit analogue outputs [34]. In addition, it had eight digital I/O lines and two 24-bit, 20 MHz counter/timers. Depending on the hard drive, the PCI-6036E could stream to disk at rates up to 200 kS/s (for its principal characteristics see the Appendix D).

Figure 3.17 PCI card

In order to connect the connector of PCI-6036E card of 68 pins to the connector of the conditioning module of 50 pins, an adapter was used [27]. The acquisition channels (0 to 4 in differentials) beginnings in the conditioning module (50 pines) correspond to the entry port of the card (68 pines) via the adapter.

---

[12] **N**ational **I**nstruments
[13] **D**ata **Acq**uisition

3.3.3 Software

To acquire and to treat the collected data a program created under NI LabView software was used. All the parameters of the test (dimensions of the sample, temperature measured etc.) were recorded. The software allowed to obtain additional information after completion of the test, such as the Young modulus or the stress and strain corresponding to rupture.

The main display of data acquisition program is presented in Figure 3.18. It shows general information about the testing sample, real-time read out values from sensors as well as the stress-strain curve. One can also adjust the frequency of acquisition in a flexible way during the test (between 20 Hz and 20 kHz) for better resolution.

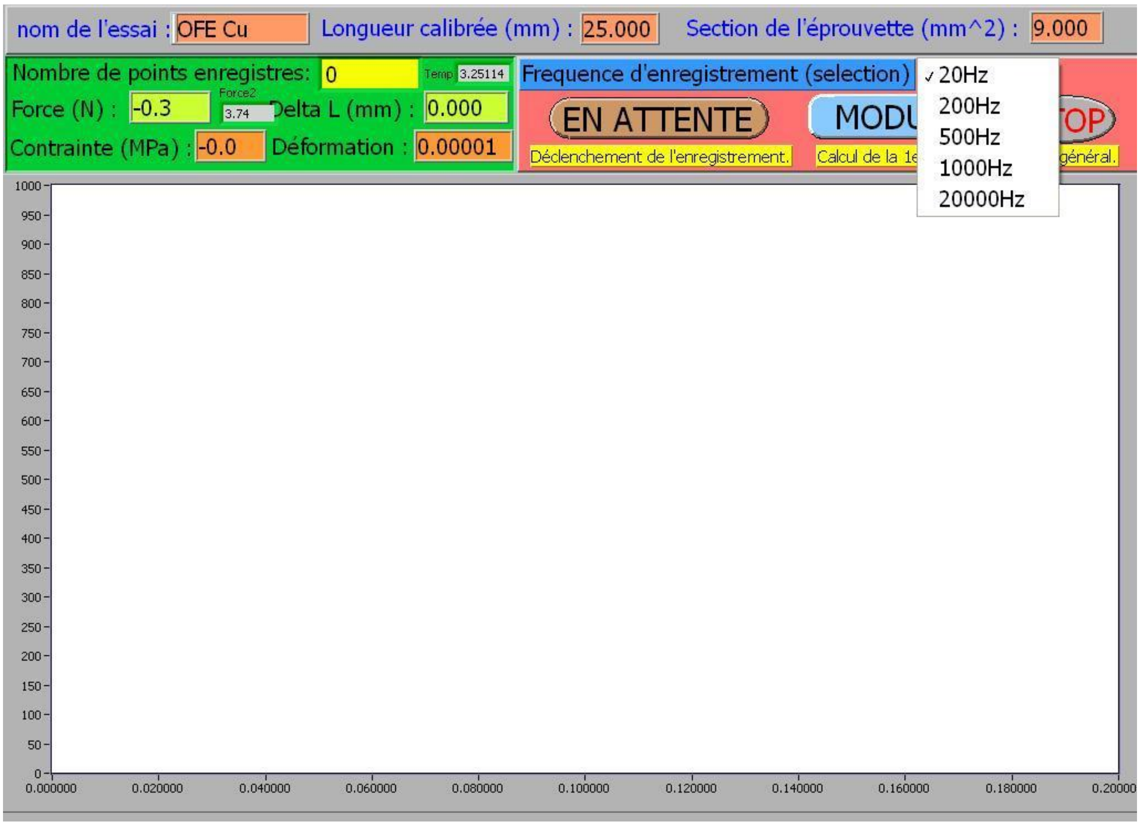

Figure 3.18 Main display of data acquisition program

Chapter 4
Experimental results obtained for typical materials used in accelerator building

4.1 OFE Copper

The first group of tested materials is pure copper. OFE[14] Copper (UNS nr C10100) in half-hard state has been studied. Chemical composition comprises 99,99% Cu (min) and further specific limits expressed in ppm for 17 elements [35]. Technical specification of the copper bar used to manufacture samples is shown in Appendix E.

OFE Copper is used in applications where the thermal conductivity is very important. It is characterized by the face centred cubic (FCC) structure. Thus, it retains toughness and ductility at cryogenic temperatures. The strengthening mechanism is limited to grain refinement and cold working [36].

Between many test results, which were obtained from pure copper samples, a selection has been carried out in order to show representative cases in the present chapter.

4.1.1 OFE Copper, sample 3

The test was made with 0.016 mm/s stroke speed. The gauge length was equal to: 16.3 mm (initial) and 19.6 mm (final). The following parameters were obtained: the Young modulus of 105 GPa, the maximum stress of 483 MPa and the yield strength of 373 MPa.

The stress-strain curve shows correspondence between the internal and the external force readouts (Fig. 4.1). One can observe growing appearance

---

[14] **O**xygen-**F**ree **E**lectronic

of serrated yielding along the stress-strain curve and rising pikes on the temperature-strain curve (Fig. 4.2).

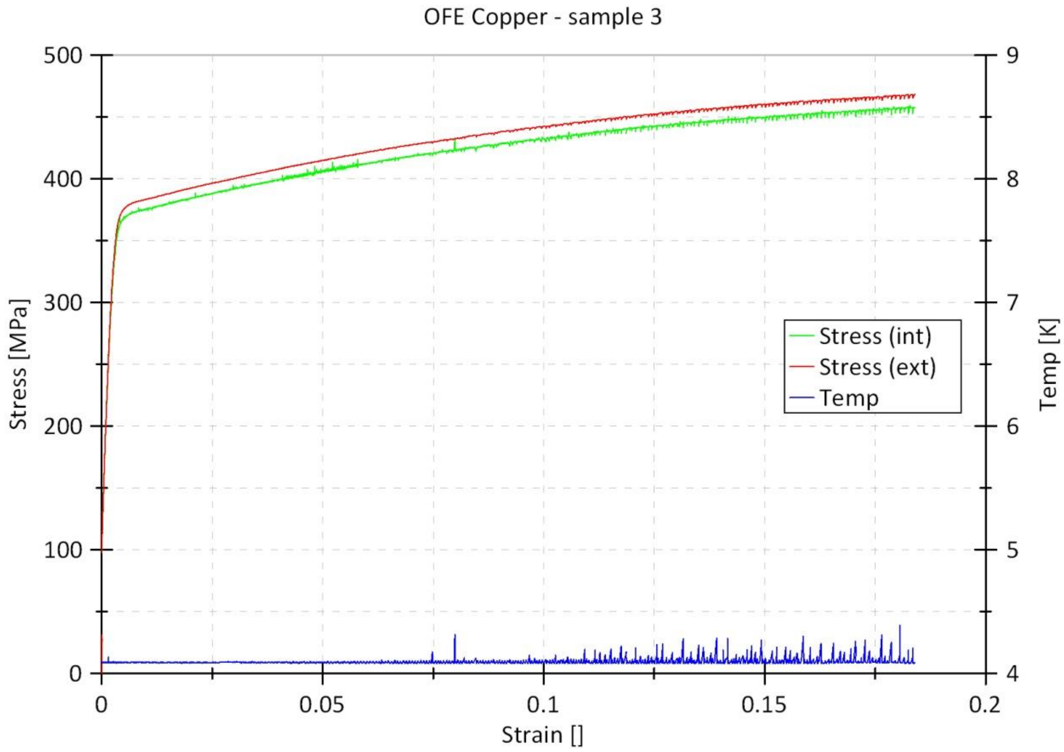

Figure 4.1 Stress-strain curve of OFE Copper – sample 3

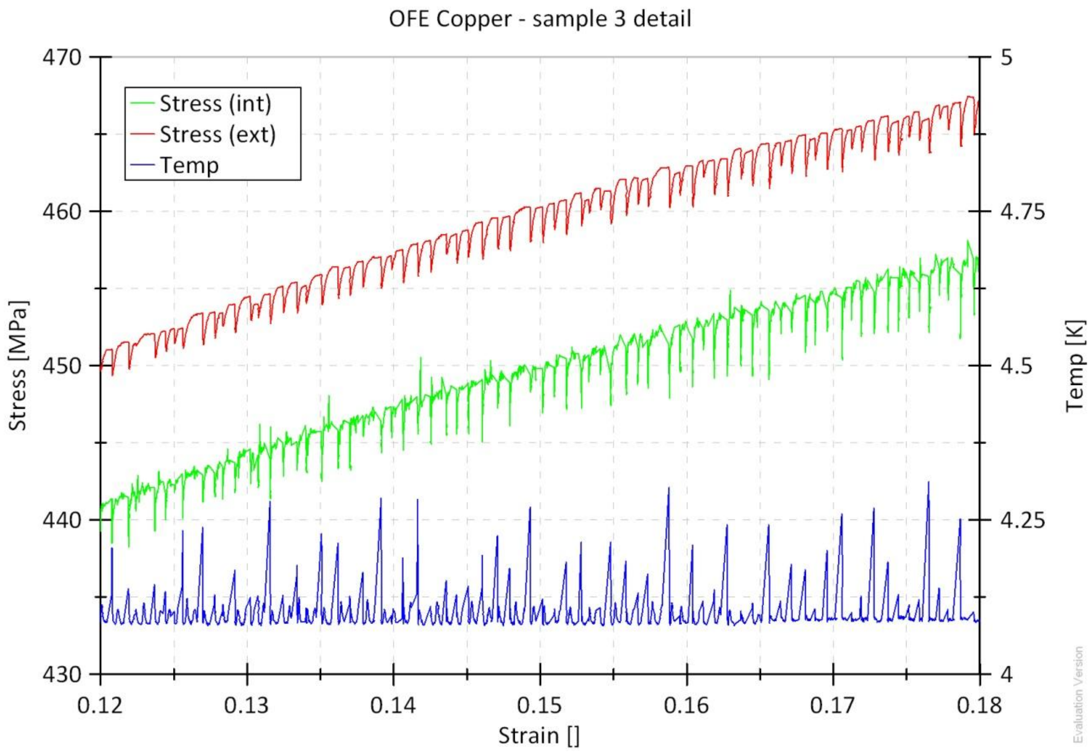

Figure 4.2 Detail view of growing serration

4.1.2 OFE Copper, sample 5

The sample was tested in two stages: the first until contraction (extensometer slid down what ended the test); the second until fracture.

The first test was carried out with 0.025 mm/s stroke speed. The gauge length was equal to: 17.5 mm (initial) and 25.4 mm (final). The following parameters were obtained: the Young modulus of 137 GPa, the maximum stress of 475 MPa and the yield strength of 324 MPa.

The second test was carried out with the same stroke speed. The gauge length was equal to: 25.4 mm (initial) and 26.6 mm (final). The following parameters were obtained: the Young modulus of 95 GPa and the yield strength of 435 MPa.

The stress-strain curve of the first test shows in a couple of places sliding of the extensometer (very strong discontinuity), especially in the end of the curve (Fig. 4.3). There are a number of areas of high frequency records where the serrated yielding can be precisely observed (Fig. 4.4). One of the serrations has been magnified and is presented in Figure 4.5.

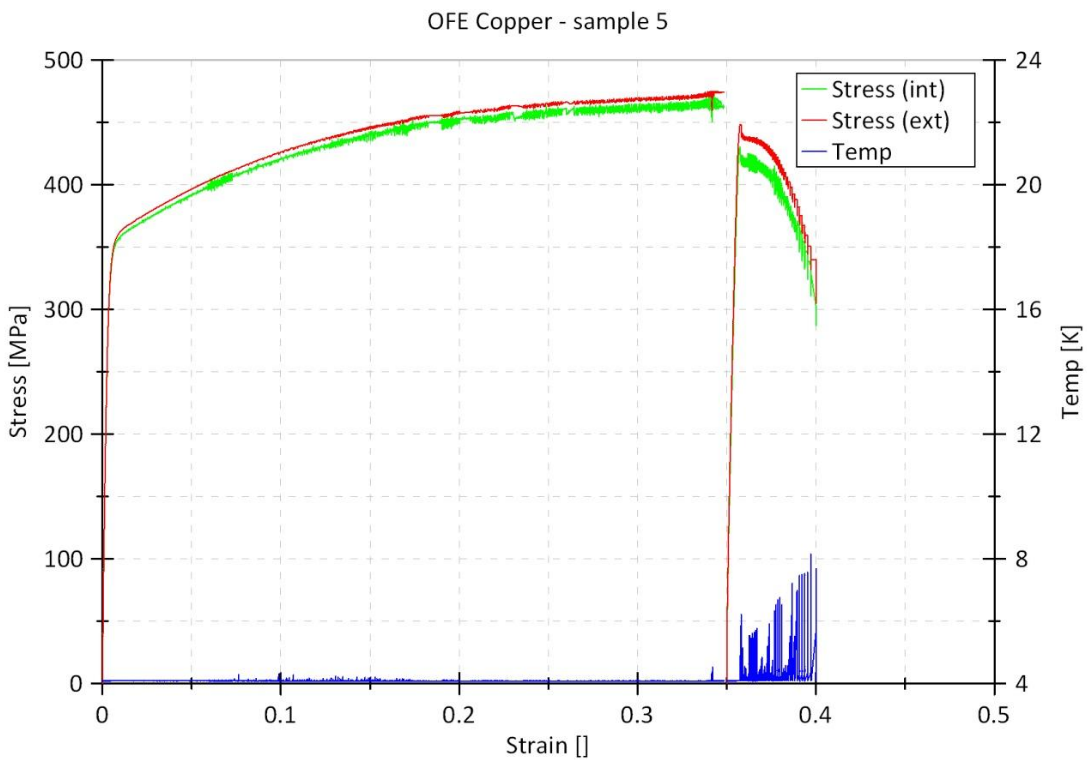

Figure 4.3 Combined stress-strain curve of OFE Copper – sample 5

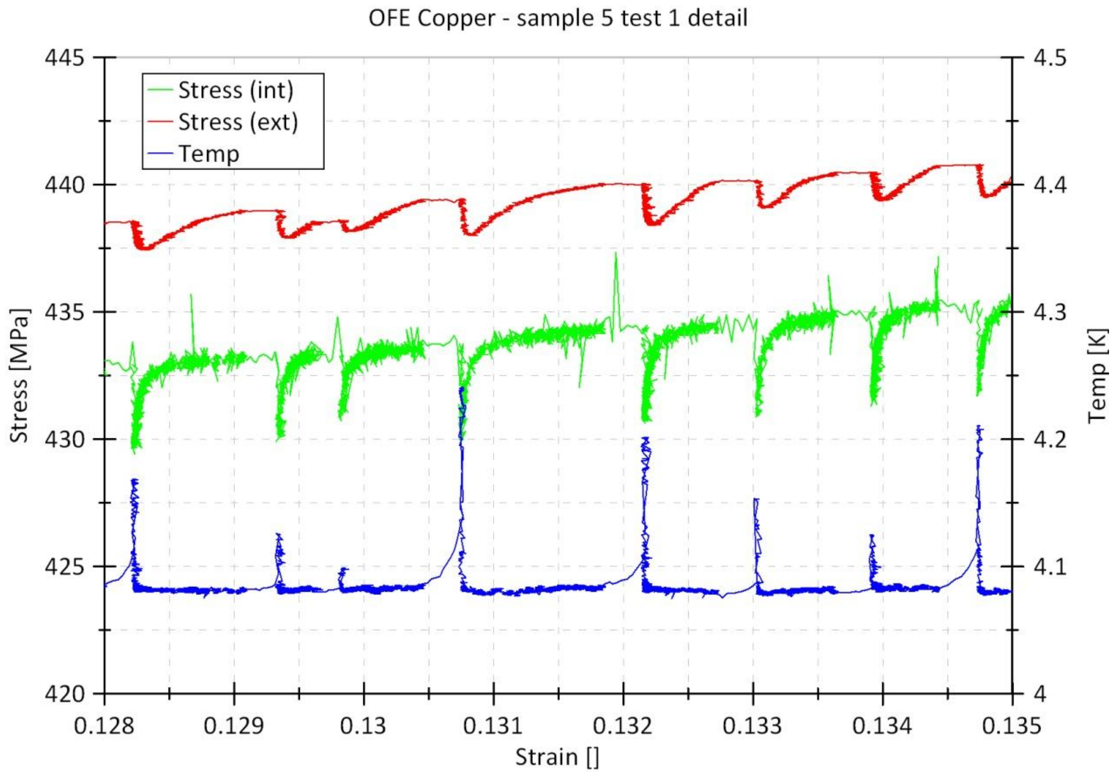

Figure 4.4 High frequency record area of serrated yielding

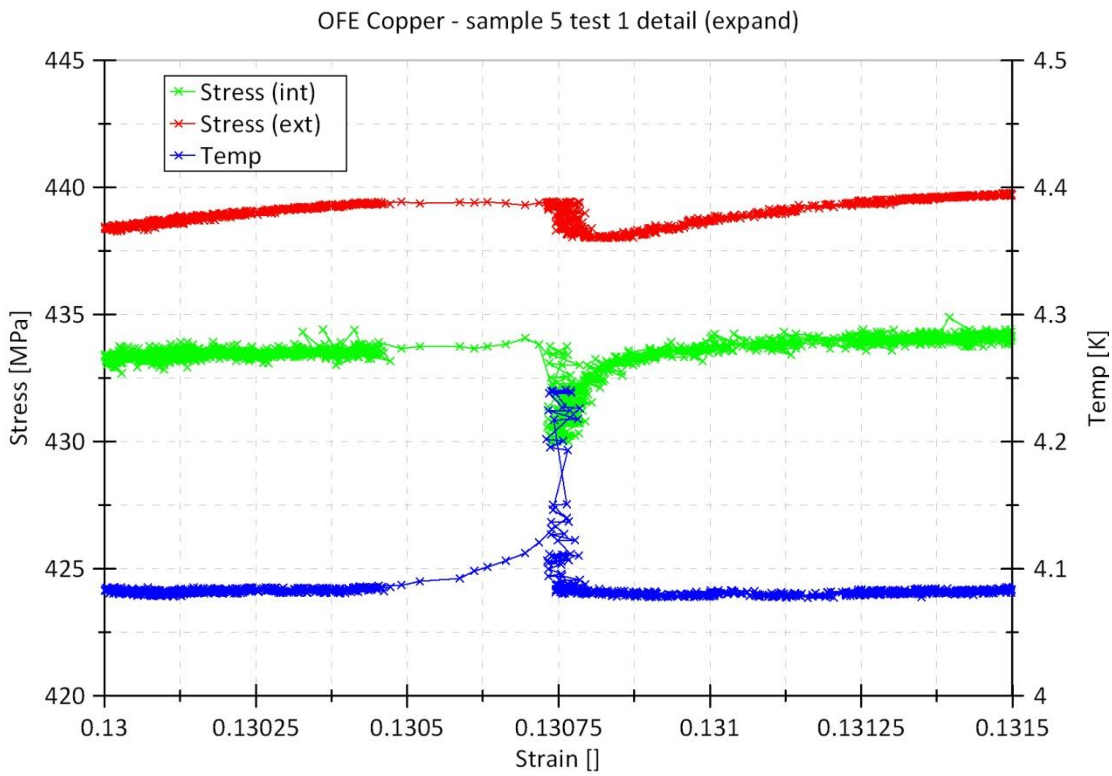

Figure 4.5 Single serration magnified with the recorded points

The second test was made after a warm up of the sample and once again setting up the extensometer and LVDT transducers. It corresponds to the necking area of the sample (Fig. 4.3). A high frequency record of serrated yielding in the necking area is presented below (Fig. 4.6).

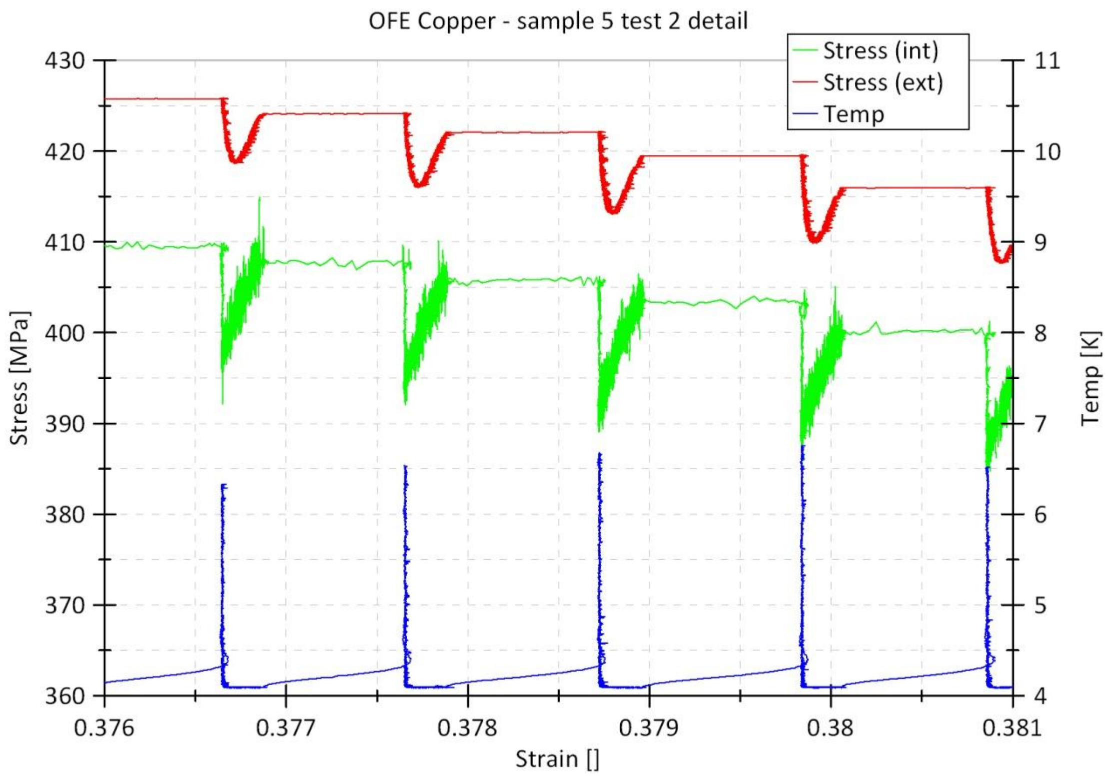

Figure 4.6 Serrated yielding in necking area of OFE Copper tensile test

Based on the testing frequency (20 kHz) an estimate of time was obtained. Taking advantage of this estimation there is a possibility to observe behaviour of each acquired parameter as a function of time (Fig. 4.7). Detailed view of serrated yielding represented as a function of time shows significant difference between the internal and the external load cell readouts (Fig. 4.8). There is obviously much faster relaxation process during jump-like deformation than previously could have been measured by means of the external load cell only.

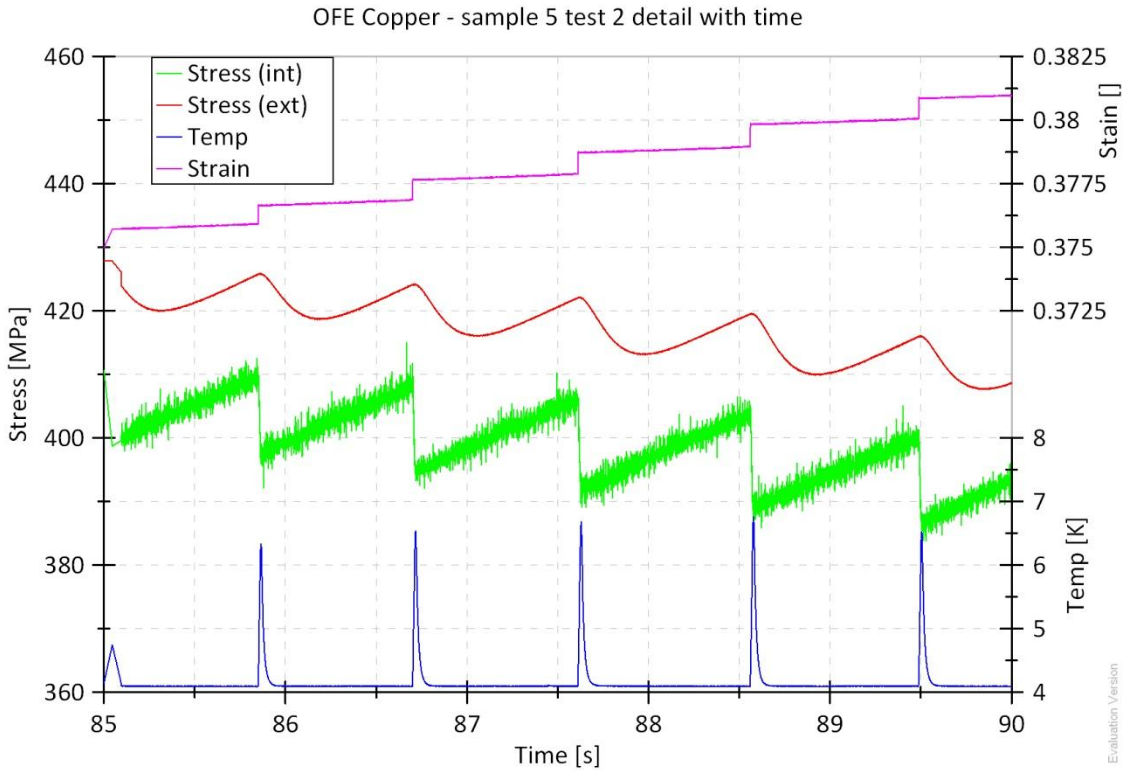

Figure 4.7 Representation of serration as a function of time

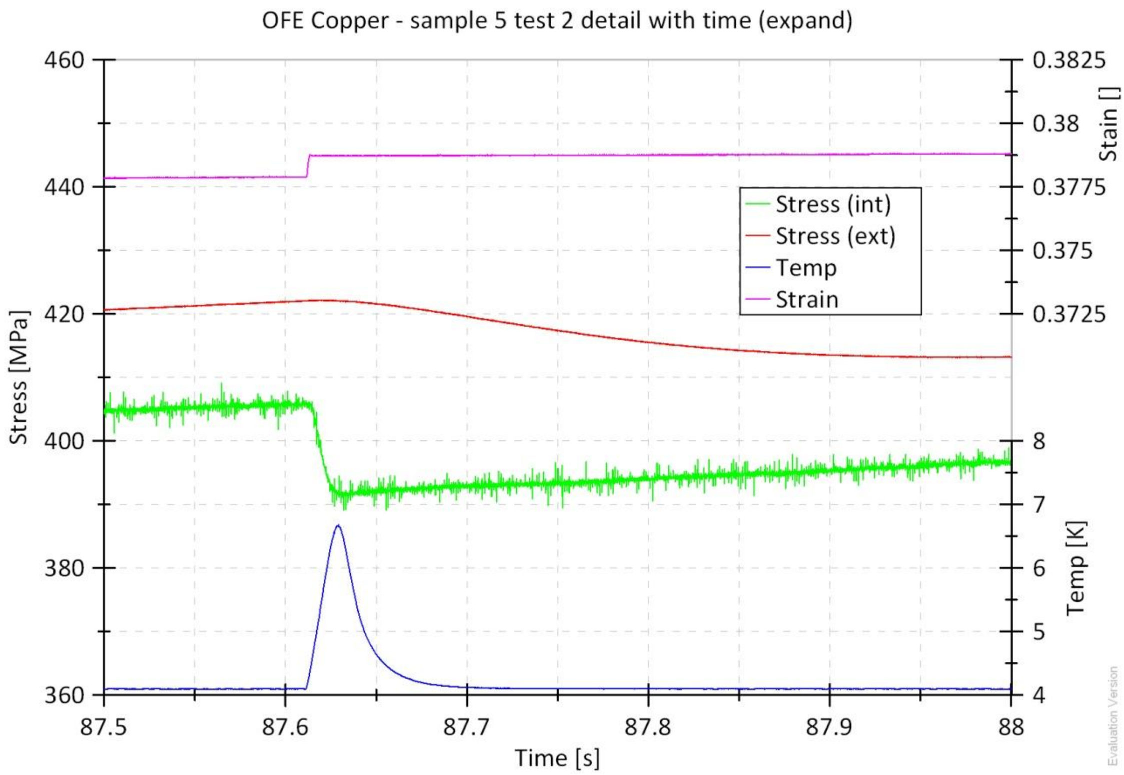

Figure 4.8 Detailed view of single serration as a function of time

4.1.3 OFE Copper, sample 6

The test is focused on checking the occurrence of serrated yielding as a function of strain rate (controlled by the stroke speed).

$$\text{Strain rate} = \frac{\text{stroke speed}}{\text{gauge length}} \tag{4.1}$$

The following parameters were obtained: the Young modulus of 102 GPa, the maximum stress of 457 MPa and the yield strength of 345 MPa.

The first test was carried out on the gauged length of 17.5 mm (initial) and 20.4 mm (final) with the stroke speed of: 0.025 mm/s until the serration appeared and then increased to 0.25 mm/s until the first unloading (Fig. 4.9). With the increasing stroke speed one could still notice serration by means of the internal load cell and the temperature readouts but the external load cell shows straight line, as if the phenomenon disappeared (Fig. 4.10).

The second test was made after warming up of the cryostat and resetting the sensors. The gauge length was of 19.4 mm (initial, corrected) and 22.0 mm (final). The test was performed with the stroke speed of 2.5 mm/s and one unloading in the middle (Fig. 4.9). One can easily observe the rise of temperature which causes complete disappearance of the serrated yielding in the tested material (Fig. 4.11).

The last test (after consecutive resetting of sensors) was made on the gauge length of 22.2 mm until fracture with primarily adjust stroke speed of 0.025 mm/s. The curve of this test shows serrations visible on the temperature sensor, by means of the internal load cell and the external load cell as well (Fig. 4.12).

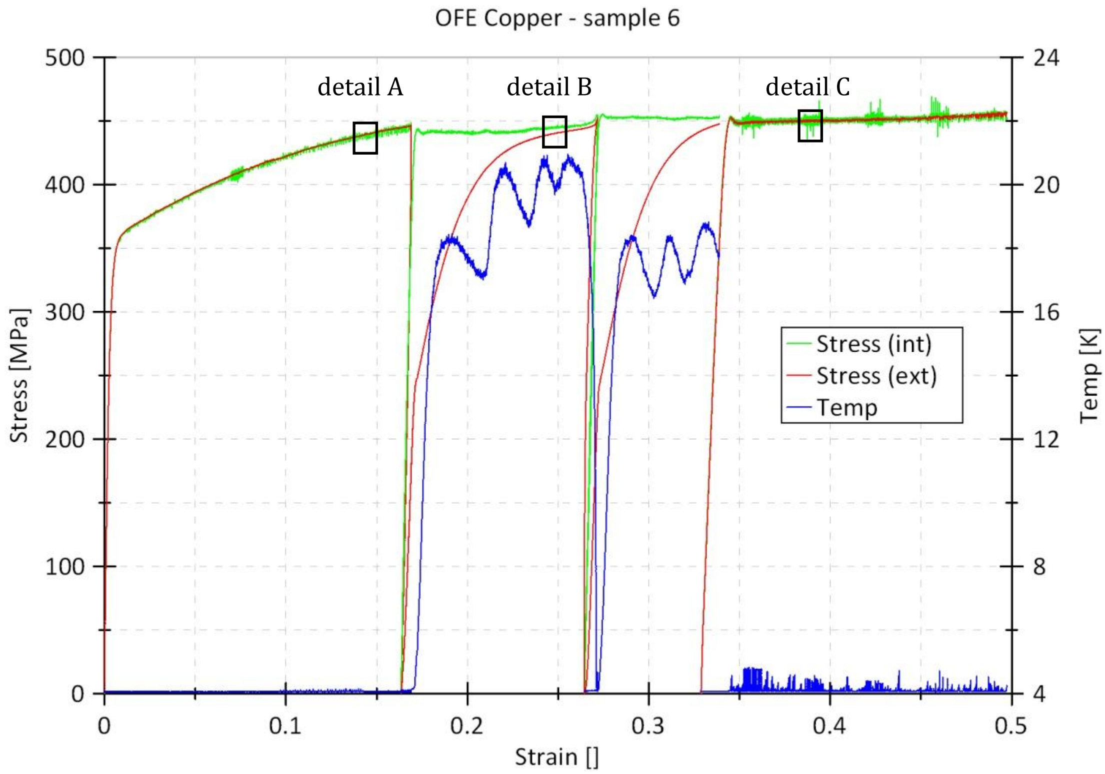

Figure 4.9 Combined stress-strain curve of OFE Copper tested with different stroke speed (strain rate) – sample 6

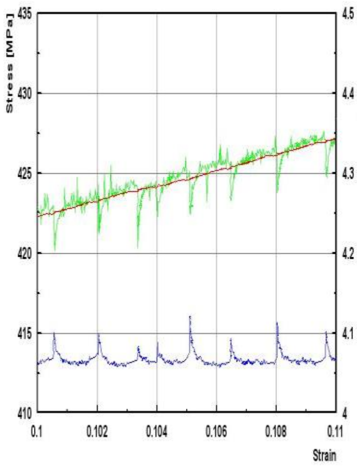

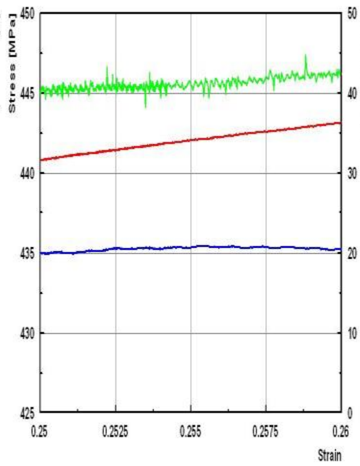

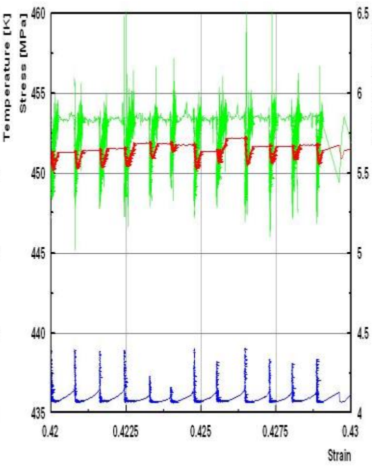

Figure 4.10 Detail A

Figure 4.11 Detail B

Figure 4.12 Detail C

4.1.4 OFE copper, sample 7

The sample was tested within three stages with many unloadings in order to measure the Young modulus which is necessary for micro-damage investigation. The tests were carried out with constant stroke speed of 0.025 mm/s. The measured gauged length was equal to:

- In the first test: initial of 14.1 mm and final of 16.6 mm,
- In the second test: initial of 16.6 mm and final of 19.2 mm,
- In the third test: initial of 19.2 mm and final of 20.5 mm.

The general parameters obtained in the course of the test are equal to: the Young modulus of 120 GPa, the maximum stress of 476 MPa and the yield strength of 354 MPa.

The origin of drop of stress on the stress-strain curve after test intervals remains to be explained (Fig. 4.13).

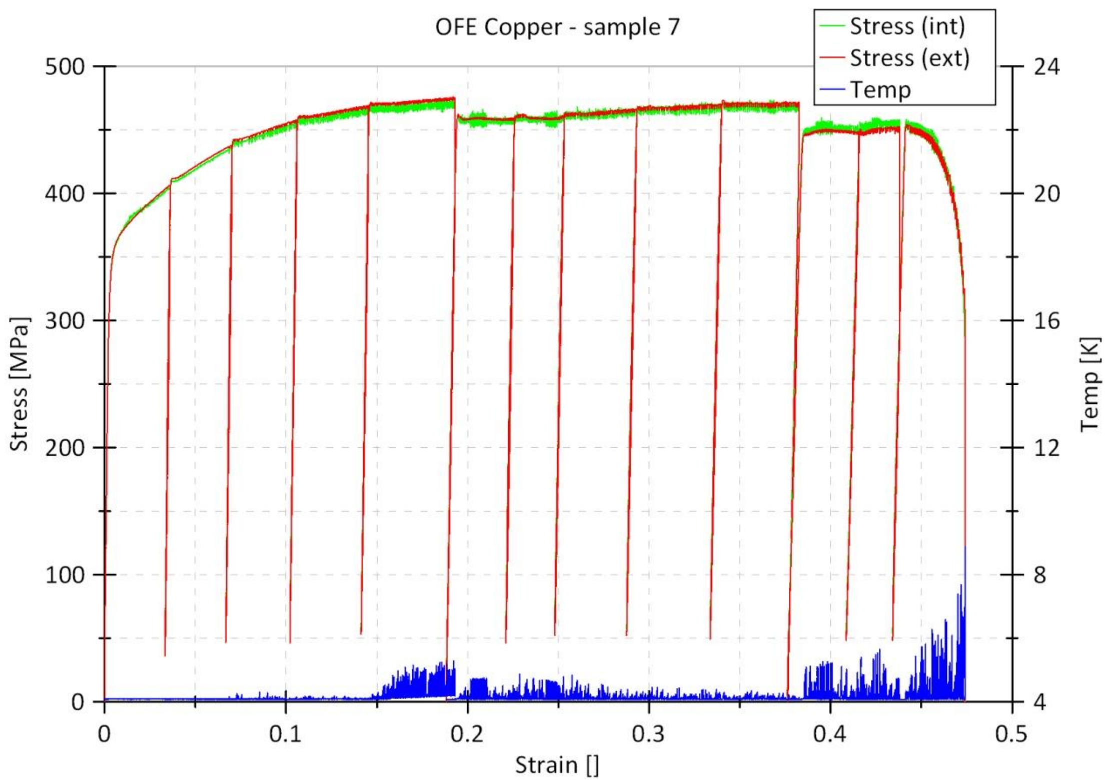

Figure 4.13 Combined stress-strain curve with unloadings for OFE Copper – sample 7

4.1.5 OFE Copper, sample 8

Another experiment with OFE Copper sample and with high frequency record areas as well as a few unloads has been carried out (Fig. 4.14).

The test was made with 0.025 mm/s stroke speed. The gauge length was equal to: 14.2 mm (initial) and 16.6 mm (final). The following parameters were obtained: the Young modulus of 110 GPa, the maximum stress of 466 MPa and the yield strength of 350 MPa.

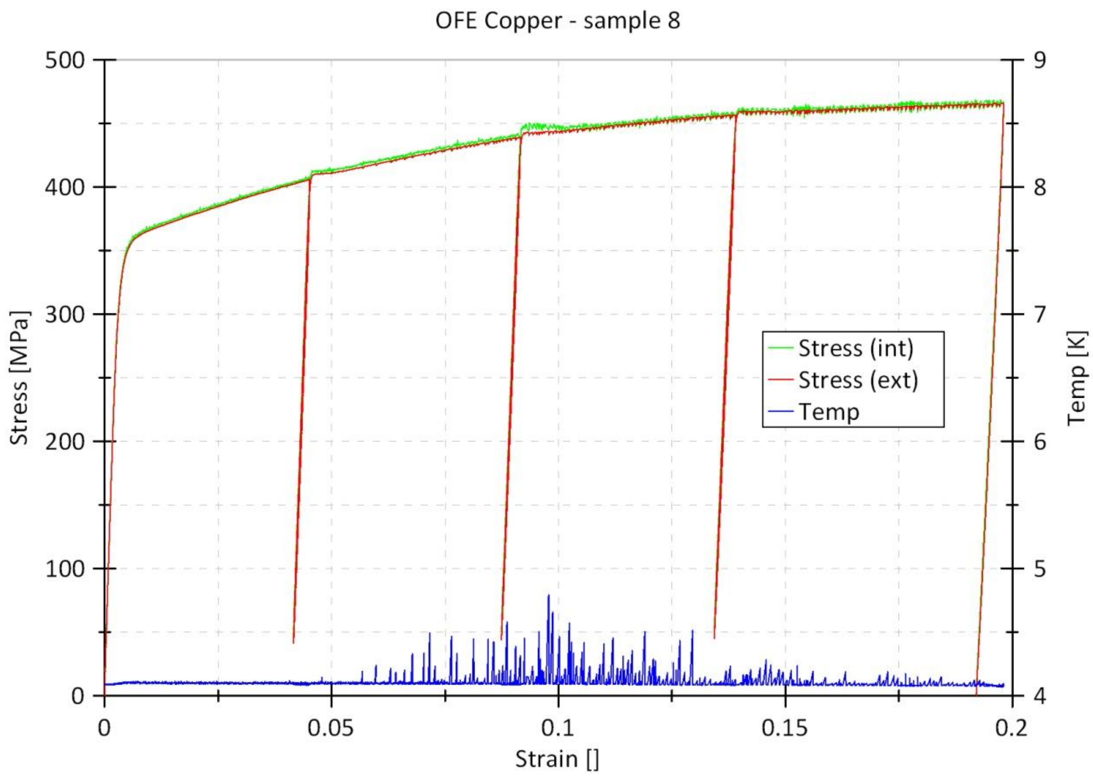

Figure 4.14 The stress-strain curve of OFE Copper – sample 8

One of the high frequency record areas, representative of serrated yielding phenomenon, was chosen and presented below (Fig. 4.15). A single jump-like deformation with the registered points representation is illustrated in Figure 4.16.

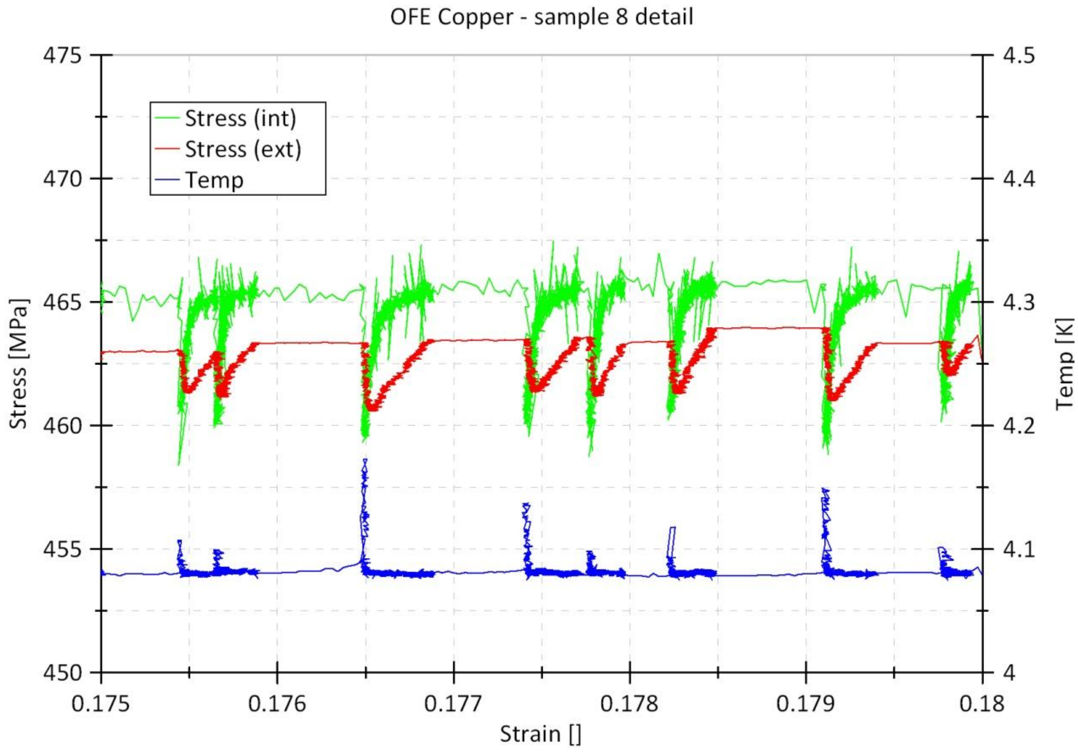

Figure 4.15 High frequency record area with serrated yielding

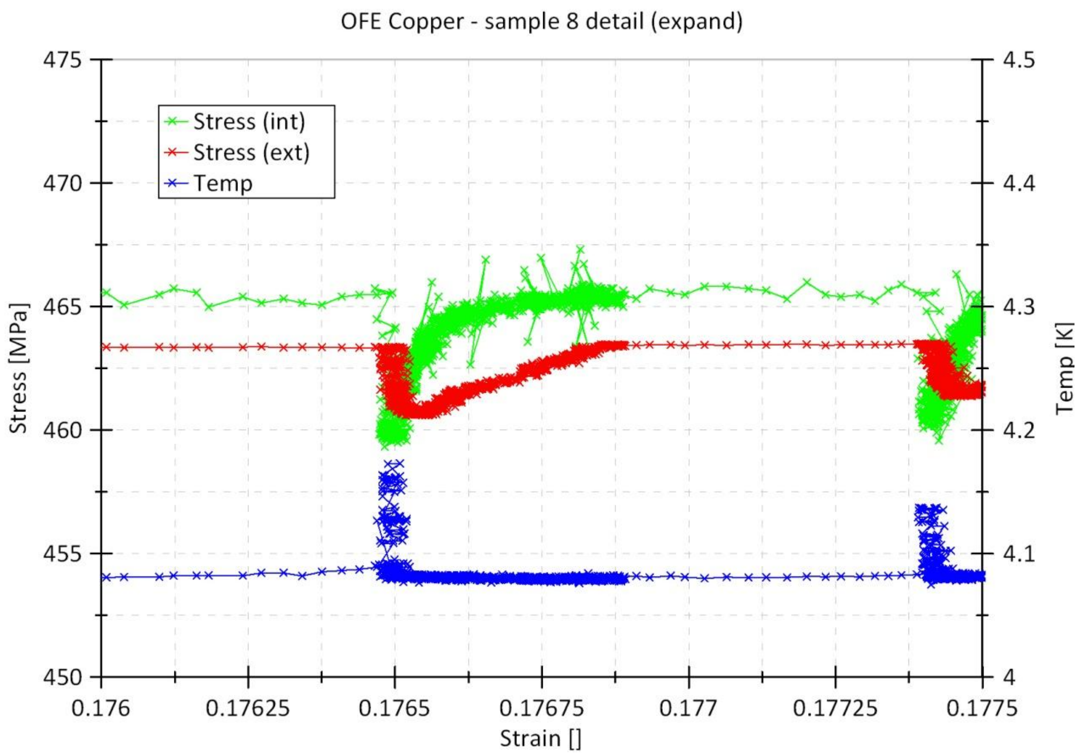

Figure 4.16 Expanded single jump-like deformation with the registered points representation

4.2 Copper-Zirconium alloys

The Copper-Zirconium alloy was the second tested material. ZHC Copper (UNS nr C15100) in two different states of work hardening: 40 and 80 % has been analysed. The main lines of chemical composition of this alloy are as follows [35]:

- 99.9 % Copper,
- 0.05-0.15 % Zirconium,
- max 0.005 % Aluminium,
- max 0.005 % Manganese,
- max 0.005 % Iron.

Al+Mn+Fe max 0.01 %

The alloys tested have significantly lower parameters of electrical and thermal conductivities but they are often used at cryogenic temperatures because of their greater strength when compared to pure copper [36]. The most representative results of testing are presented below.

4.2.1 ZHC Copper, C15100 – 40%

The Copper-Zirconium alloy with 40% CW[15] was tested within two stages, with the stroke speed of 0.025 mm/s in both cases. The measured gauge length was equal to:

- in the first test: initial of 14.1 mm and final of 16.6 mm,
- in the second test: initial of 16.6 mm and final of 19.4 mm.

The general parameters obtained are as follows:

- the Young modulus of 119 GPa,
- the maximum stress of 502 MPa,
- the yield strength of 336 MPa.

The stress-strain curve in this test (Fig. 4.17) contains unloading-uploading hysteresis loops and high frequency record areas of serrated yielding (Fig. 4.18).

[15] **C**old **W**ork

A short part of this curve was expanded to show single serration with the registered points representation (Fig. 4.19).

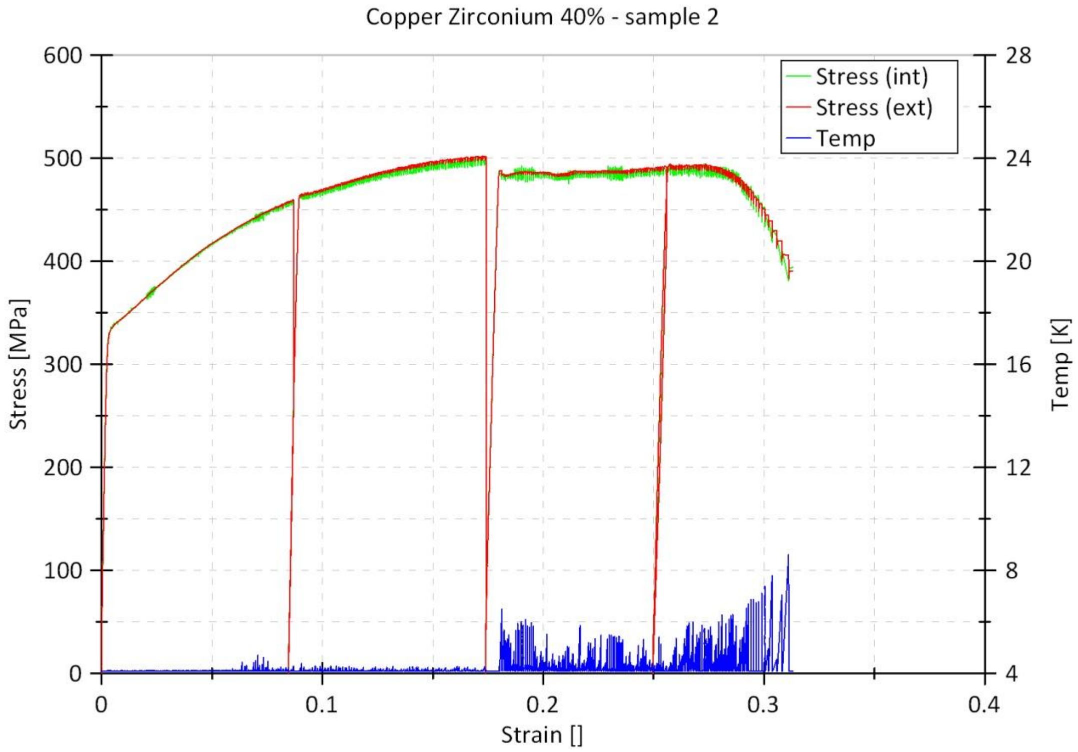

Figure 4.17 The stress-strain curve of ZHC Copper 40% CW – sample 2

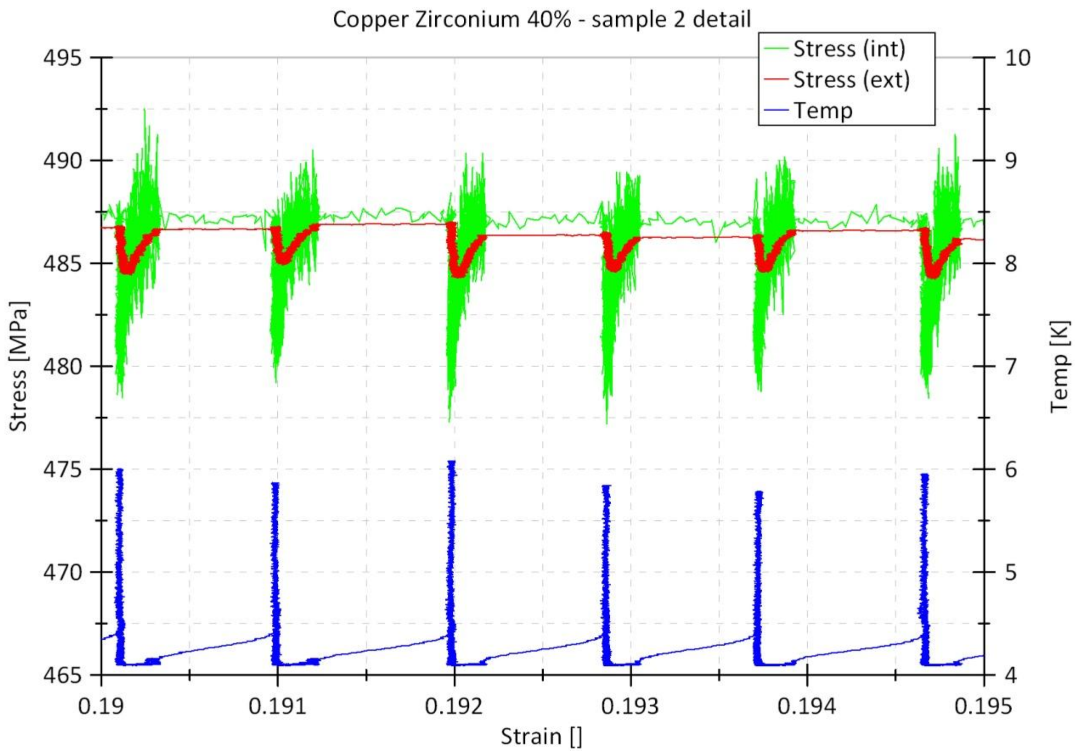

Figure 4.18 Representative high frequency record area of serration

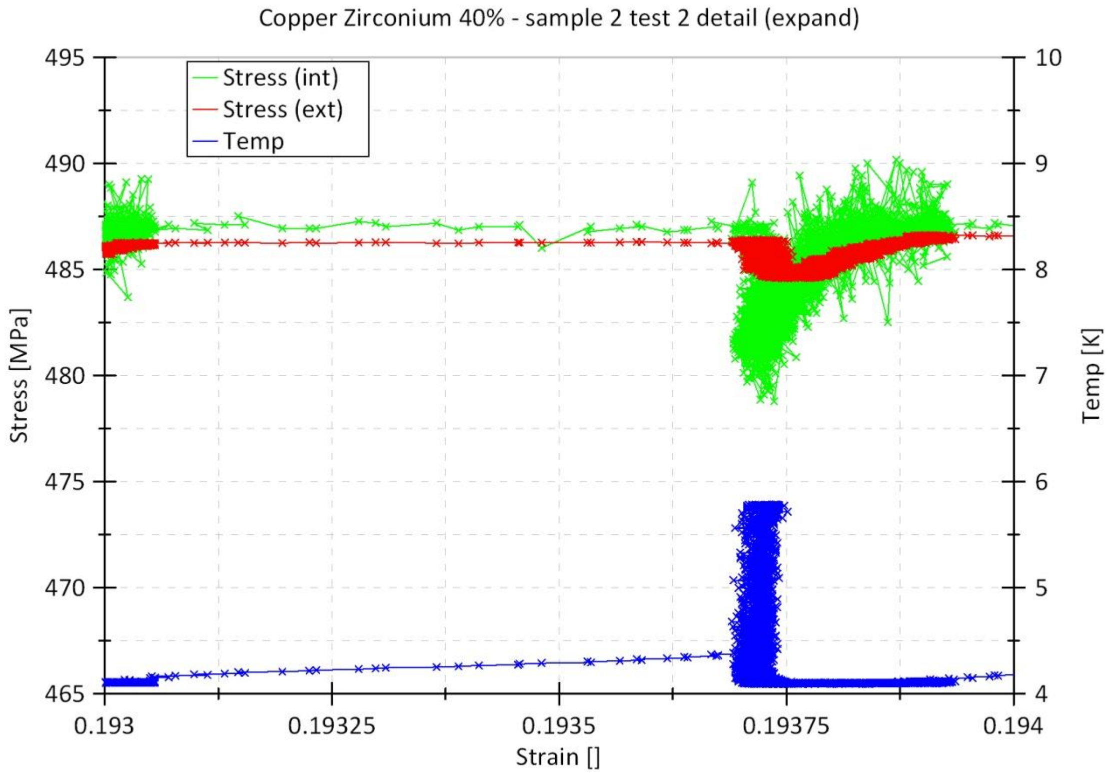

Figure 4.19 Single jump-like deformation with the registered points representation

4.2.2 ZHC Copper, C15100 – 80%

Next material tested was Copper-Zirconium alloy with 80% CW. The test was carried out with the stroke speed of 0.025 mm/s. The measured gauge length was equal to: initial of 14.1 mm and final of 16.6 mm. The following general parameters were obtained:

- the Young modulus of 116 GPa,
- the maximum stress of 560 MPa,
- the yield strength of 401 MPa.

The stress-strain curve in this test (Fig. 4.20) contains the unloading-uploading hysteresis loops and high frequency record areas of the serrated yielding phenomenon (Fig. 4.21), similar to those obtained from ZHC Copper with 40% CW. The short part of this curve was again expanded to show single serration with the registered points representation (Fig. 4.22).

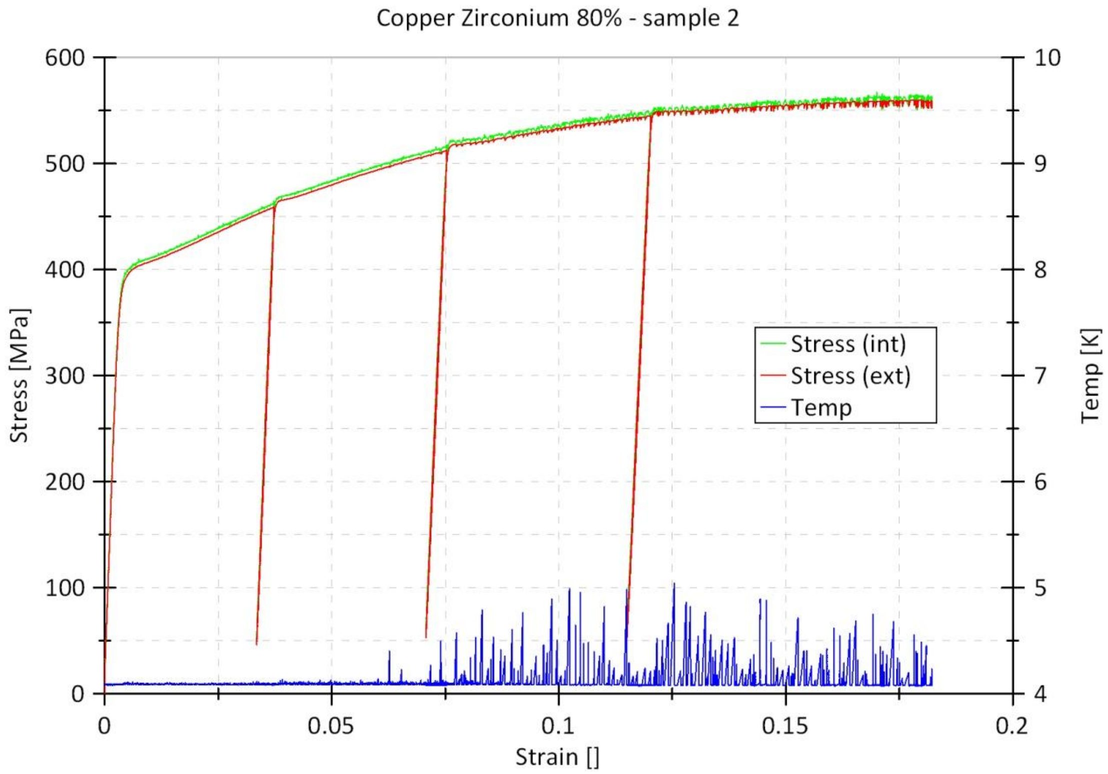

Figure 4.20 The stress-strain curve of ZHC Copper 80% CW – sample 2

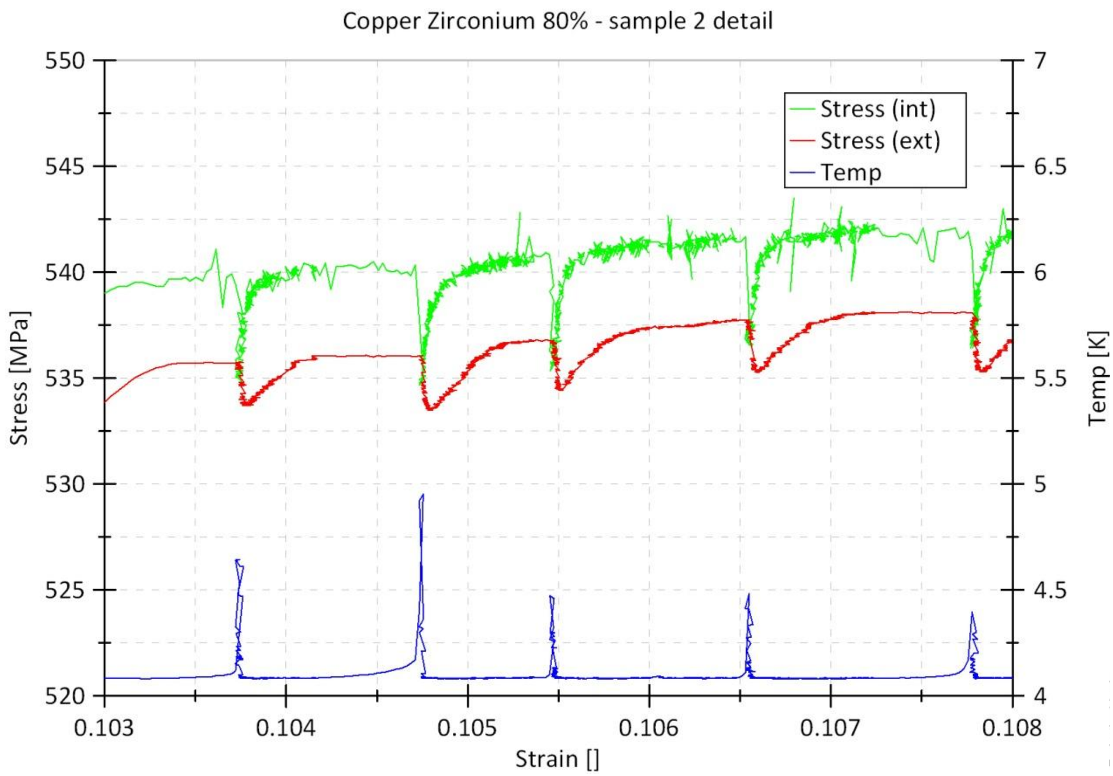

Figure 4.21 Representative high frequency record area of serration

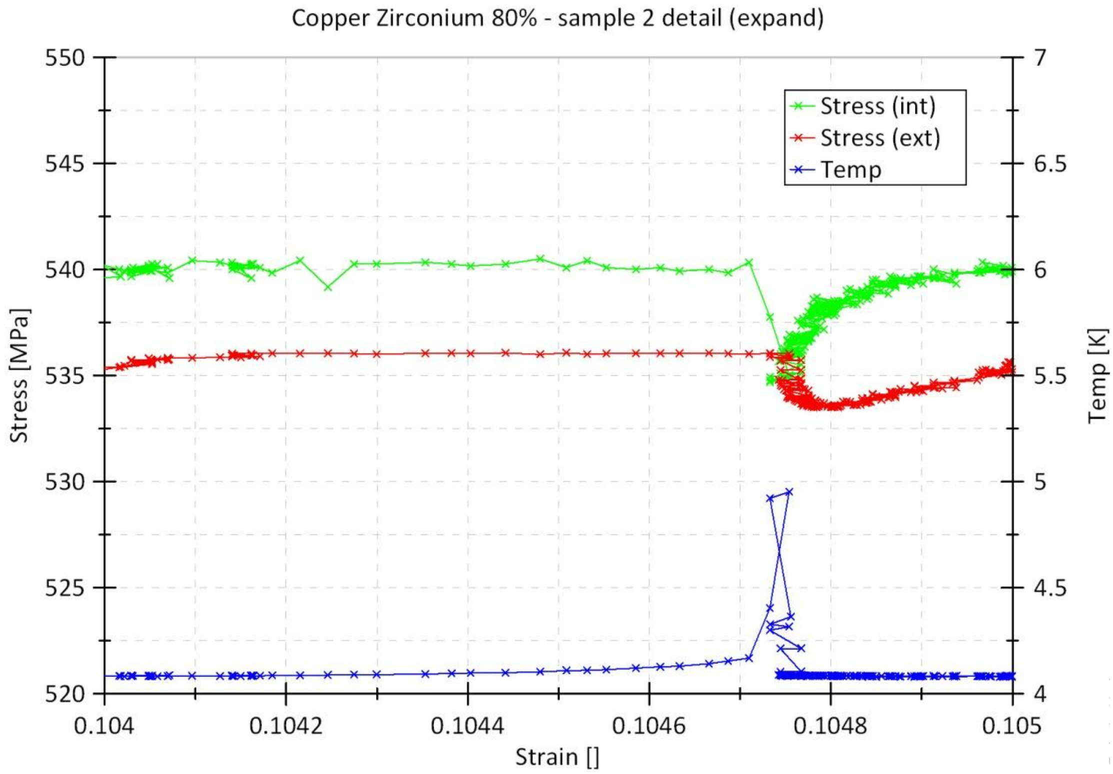

Figure 4.22 The jump-like deformation with the registered points representation

4.3 Stainless Steel 316 LN

The last material tested was the annealed stainless steel 316 LN (UNS nr S31653). The composition of the steel alloying elements is listed below:

- 18% Chromium,
- 12 % Nickel,
- 3 % Molybdenum,
- 2 % Manganese,
- 0.75 % Silicon,
- 0.10 % Nitrogen,
- 0.045 % Phosphorus,
- 0.03 % Carbon,
- 0.03 % Sulphur.

The stainless steel 316 LN is characterized by an austenitic structure and – if not strained - maintains it down to the cryogenic temperatures. It remains highly resistant to the corrosion because of its low carbon content and it is characterized by higher (than 316 alloy) yield and tensile strength thanks to the nitrogen addition.

The test was carried out with the stroke speed of 0.025 mm/s. The measured gauge length was equal to: initial of 25.0 mm and final of 27.6 mm. The general parameters obtained in the course of test are as follows:

- The Young modulus of 185 GPa,
- The maximum stress of 1410 MPa,
- The yield strength of 1059 MPa.

The stress-strain curve in this tensile test shows larger difference between readouts from the internal and the external load cells than in all previous experiments (Fig. 4.23). It is accurately shown in the detailed curve that presents single serration recorded in high frequency mode (Fig. 4.24).

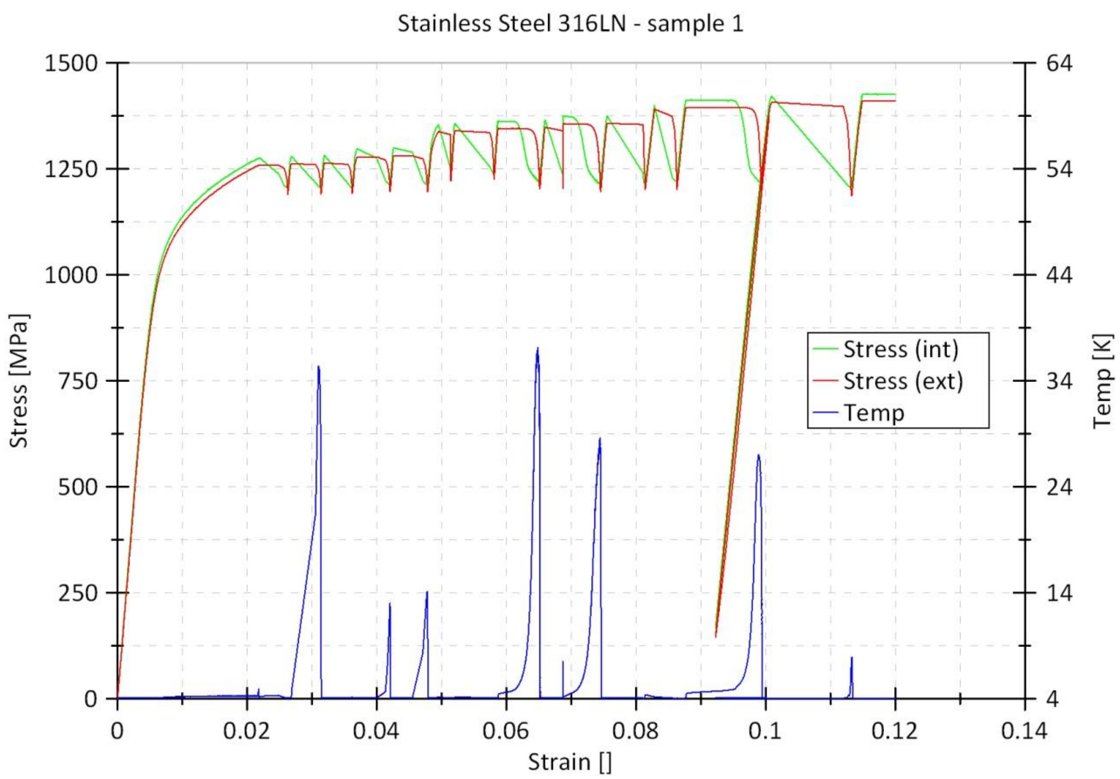

Figure 4.23 The stress-strain curve of stainless steel 316LN – sample 1

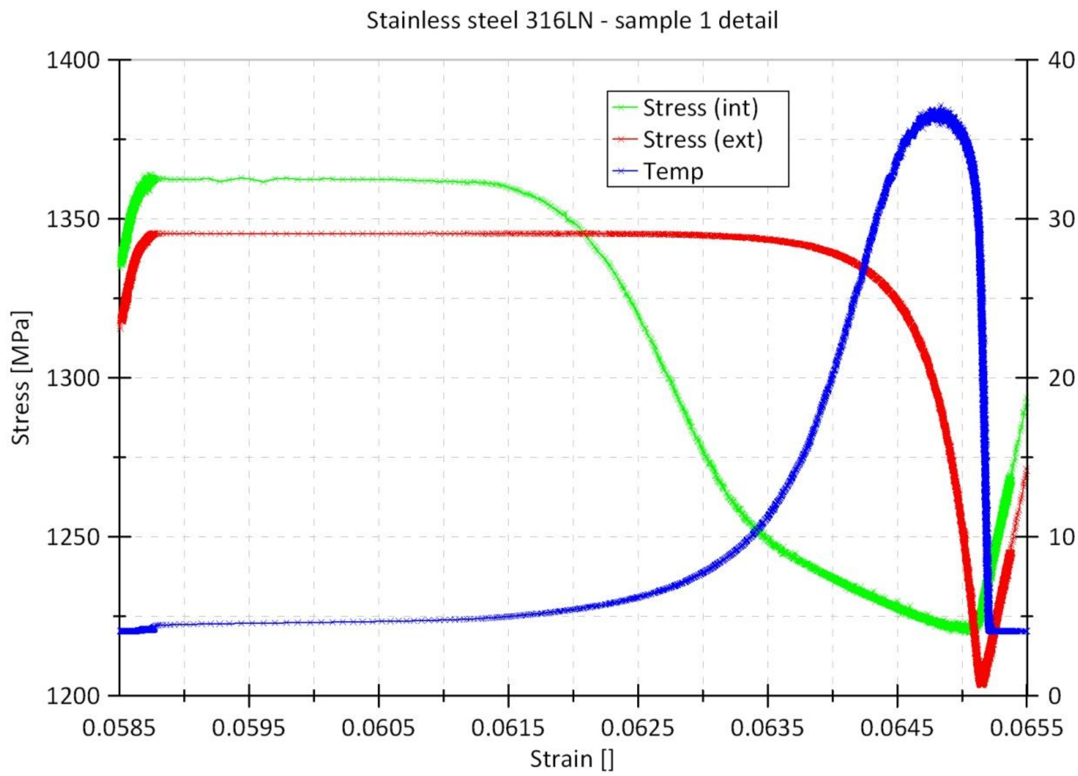

Figure 4.24 High frequency record of detail of jump-like deformation in stainless steel 316 LN

It is worth pointing out, that the stainless steel shows different type of plastic flow discontinuities when compared to copper. In particular, the size of serrations on the strains scale is larger. Each serration follows similar four stage pattern (Fig. 2.1): elastic response (1), plastic flow (2), drop of stress measured in microseconds (3) and stress relaxation measured in milliseconds (4). Also, each serration is accompanied by a significant increase of temperature from 4.2 K up to some 40 K, which is a consequence of thermodynamic instability at very low temperatures.

Chapter 5

Validation of kinetic laws

5.1 Discontinuous plastic flow

Serrated yielding observed at low temperatures and in the framework of sufficiently high strain rate during monotonic loading is recorded as frequent abrupt drops of stress as a function of strain. The mechanism of discontinuous plastic flow can be explained by means of dislocation pile-ups formation at strong obstacles (such as the Lomer-Cottrell locks) during the strain hardening process [37]. It takes place below the threshold temperature of T_0 or T_1 where the edge dislocations have predominant character and cannot easily leave the pile-up by the mechanism of cross-slip. The motion of newly created dislocations is blocked by the back stresses of the pile-ups. Thus, at the head of dislocation pile-up the local shear stress (proportional to the number of dislocations in the pile-up) may collapse the obstacle by reaching the level of cohesive strength and turn it into a glissile dislocation. As a result of this local event similar effects can be triggered in other dislocation pile-ups and the final result is massive and has a collective character. At cryogenic temperatures where very high stresses are expected this avalanche-like process is followed by a spontaneous generation of dislocations by rapidly increasing number of sources. This leads to a rapid local deformation and the load drops observed in the stress-strain curve (Fig. 5.1a). During low temperature tensile test the barrier crossing by dislocation pile-ups is manifested by acoustic effects of "dry" sounds emitted by the specimen.

Each load drop is accompanied by local increase of temperature, related to the dissipation of plastic power and "thermodynamic instability". It seems that the temperature increases dramatically when the abrupt relaxation of stress begins. However, as the temperature of the sample is usually measured at the surface, it might be delayed by thermal diffusivity (if the phenomenon does not occur in the proximity of the surface) and by the time response of the thermometer.

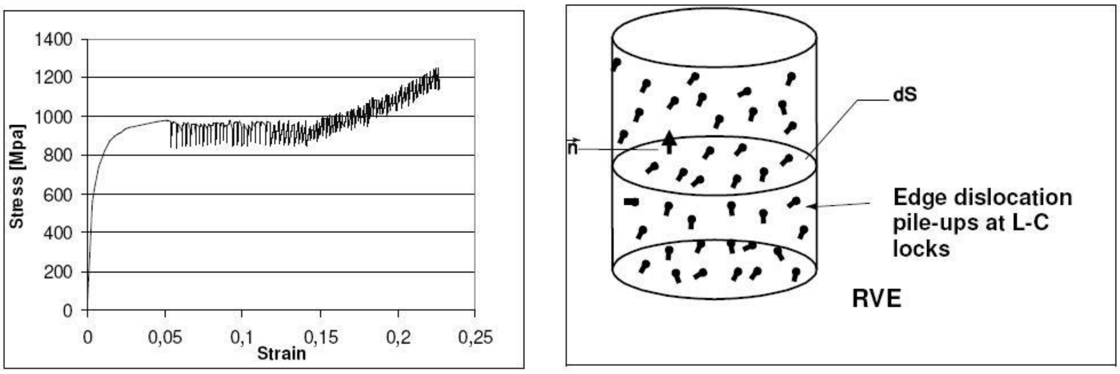

Figure 5.1 (a) Serrated yielding in FCC metals. (b) RVE and dislocation groups localized at the Lomer-Cottrell locks [37]

In some cases an upper limit in terms of the strain rate is reported for serrated yielding. In reality this is a "pseudo" limit since for sufficiently high strain rates the temperature of the specimen starts to diverge and remains no longer in equilibrium with the bath (reference temperature).

The main function that reflects the readiness of lattice with respect to discontinuous plastic flow is the density B of the dislocation groups (located at the Lomer-Cottrell locks). The RVE containing the dislocation groups is shown in Figure 5.1b. It is assumed that the increment of B is strictly related to the increment of accumulated plastic strain (Odqvist parameter):

$$dp = \sqrt{\frac{2}{3} d\underline{\underline{\varepsilon}}^P : d\underline{\underline{\varepsilon}}^P} \tag{5.1}$$

Increasing intensity of plastic flow generates more barriers for the motion of dislocations. Therefore, the following kinetic law of evolution for the density of the Lomer-Cottrell locks was postulated [37]:

$$\dot{B} = F_{LC}^{+}\left(\rho, T, \underline{\underline{\sigma}}\right) \dot{p} H(p - p_{LC}) \tag{5.2}$$

where F_{LC^+} is a function of density of dislocations ρ , temperature T and the level of stress σ whereas p_{LC} represents a threshold above which the Lomer-Cottrell barriers massively develop. For an isothermal process and small variation of the flow stress a simple linear representation can be obtained [37]:

$$dB = F_{LC}^{+} dp\ ; p \geq p_{LC} \tag{5.3}$$

As the constitutive model of serrated yielding is currently under development, the identification of suitable parameters will be carried out as soon as the model is available [37].

5.2 Plastic strain induced γ-α' phase transformation

Transformation kinetics has been developed by Olson and Cohen [38]. The authors attribute the strain-induced martensite nucleation sites to the shear-band intersections (the shear-bands being in the form of ε' martensite, mechanical twins or stacking-fault bundles). The analysis leads to the following equation for the volume fraction of martensite versus plastic strain [25]:

$$\xi_{\alpha'} = 1 - exp\{-\beta[1 - exp(-\alpha\varepsilon^P)]^n\} \tag{5.4}$$

where α represents the rate of shear-band formation, β represents the probability that a shear-band intersection will become a martensite site and n is a fixed exponent. The transformation curves (volume fraction of martensite versus plastic strain) show a typical sigmoid shape with saturation level below 100 % (Fig. 5.2). Olson and Cohen developed one-dimensional model for the kinetics of martensitic transformation, called OC model. The evolution of the volume fraction of martensite as a function of plastic strain is derived by considering the shear band formation, the probability of shear-band intersections and the probability of an intersection generating a martensitic embryo. In this model, the temperature and the plastic strain control the martensite evolution only. Different improvements have been brought to this model, covering the influence of the stress state [39] and the strain rate [40]. However, a considerable number of parameters have to be identified for these models. In the current Thesis, a simplified model - developed by Garion and Skoczeń [22] for cryogenic applications – is recalled. The volume fraction of martensite ξ is presented in the following form:

$$\xi = \xi\left(\varepsilon^{p}, T, \underline{\underline{\dot{\varepsilon}}}^{p}, \underline{\underline{\sigma}}\right) \tag{5.5}$$

where $\underline{\underline{\dot{\varepsilon}}}^{p}$ denotes the plastic strain rate and $\underline{\underline{\sigma}}$ is the stress tensor. Under isothermal conditions and for a given strain rate, the classical sigmoid curve has the following form (Fig. 5.2):

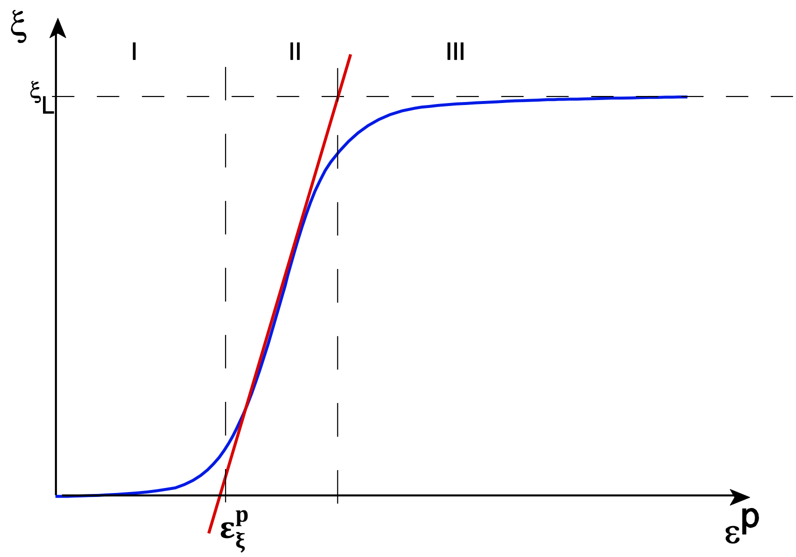

Figure 5.2 Volume fraction of martensite versus plastic strain at cryogenic temperatures (4K, 77K) [25]

The curve is decomposed into 3 phases: *phase I* corresponds to a nonlinear increase of the martensite content as a function of the plastic strain, *phase II* - the α' volume fraction (ξ) is linearly related to the plastic strain (ε^{p}) and *phase III* corresponds to a saturation effect (ξ_L). A simplified evolution law for the martensite content has been proposed for the phase II under the following form:

$$\dot{\xi} = A\left(T, \underline{\underline{\sigma}}, \underline{\underline{\dot{\varepsilon}}}^{p}\right)\dot{\varepsilon}^{p} H\left[\left(\varepsilon^{p} - \varepsilon^{p}_{\xi}\right)(\xi_L - \xi)\right] \tag{5.6}$$

where A is function of temperature, stress and plastic strain rate, ε_{ξ}^{p} is the plastic strain threshold (to trigger formation of martensite), ξ_L is the martensite content limit, over which the martensitic transformation rate is considered equal to 0. Finally, H represents the Heaviside function:

$$\begin{cases} H(x) = 1 \; if \; x \geq 0 \\ H(x) = 0 \; if \; x < 0 \end{cases} \tag{5.7}$$

The identification process described below has been carried out at CERN several years ago [41]. Samples issued from two different heats of 316L have been studied, corresponding to two different thicknesses (0.15 and 0.2 mm). The chemical composition is reported in Table 1. The Ni content for 0.25 mm thick plates is equal to 11.03 %. As the Ni is an austenite-forming element, it improves the stability of austenite under thermo-mechanical cycling. Mo content is equal to 2.032 % and 1.97 %, respectively. This constituent increases the stability of stainless steel with respect to the strain induced martensitic transformation.

Element	Thickness 0 .15 mm content %	Thickness 0 .25 mm content %
C	0.027	0.029
Si	0.596	0.492
Mn	1.557	0.872
P	0.022	0.025
S	0.0009	0.0022
Cr	17.99	17.91
Ni	10.29	11.03
Mo	2.032	1.97
Co	0.122	0.195
N	0.0075	0.0074

Table 5.1 Results of chemical analysis for the fine gauge 316L plates, thickness 0.15 and 0.25 mm

It is worth pointing out, that the material is stable with respect to the spontaneous phase transformation down to 0 K.

The tensile tests (Fig. 5.3) were aimed at understanding the behaviour of austenite/martensite two-phase composite obtained by plastic stretching of 316 L stainless steel at cryogenic temperatures. It is fundamental to identify the value of strain (threshold) where the martensitic transformation begins. The rate of martensitic transformation was assessed at 4.2 K for different strain levels: 5, 10 and 20%. At each deformation level the samples were removed from the helium bath in order to perform the measurement of magnetic permeability and to deduce the amount of α' martensite formed in the sample. Tensile testing was performed by means of flat specimens (section 0.45 or 0.75 mm2). A universal electromechanical testing machine UTS 200.4 (load cell 25 kN) was applied. Two different extensometers were used: an inductive sensor for the elastic range (Sensorex SX 9W3) and a carbon potentiometer for the plastic range (MCB RX 13-50). The tests were kinematically controlled.

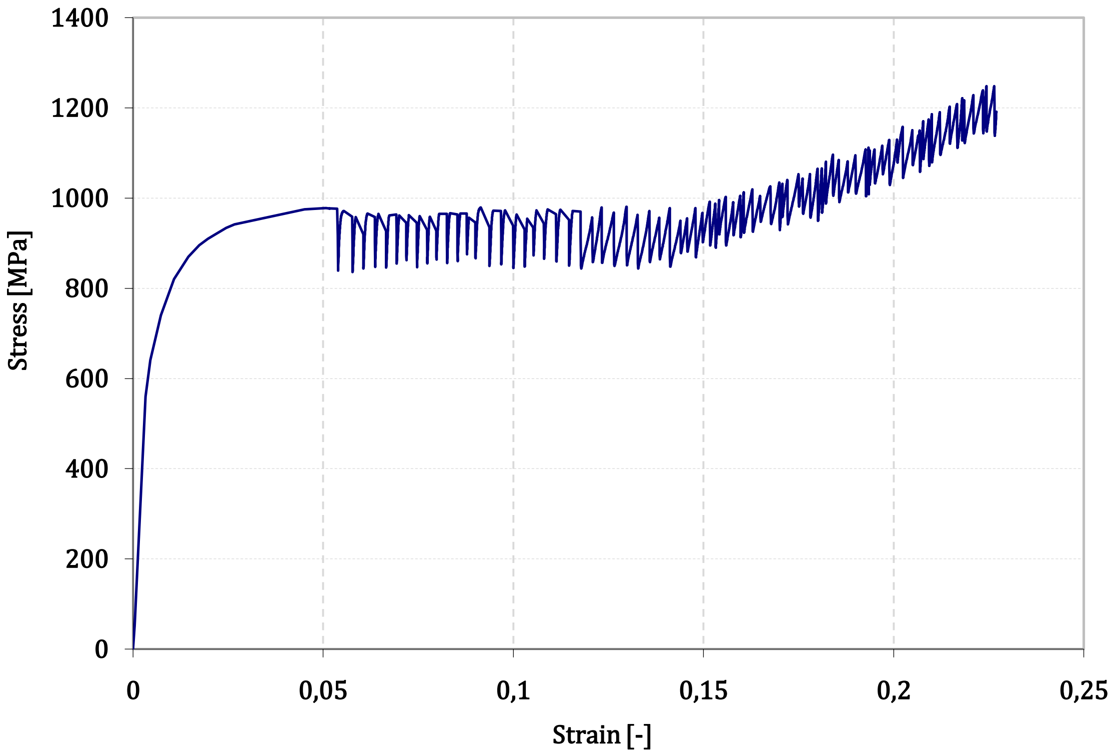

Figure 5.3 Uniaxial test of stainless steel 316L at 4.2 K

The volume fraction of martensite is quantified by suitable magnetic methods. The set-up, used for magnetization measurements, consists of a superconducting coil. It is equipped with temperature stabilization and relevant instrumentation to measure the magnetization (M) and the magnetic field (H). Measuring the magnetic flux induced by the sample inside the measuring coil enables quantification of the magnetization. The flux is calculated on the basis of the reciprocity theorem. Two different methods have been used to measure the magnetic flux: the first method called the VSM (Vibrating Sample Magnetometer), for which a periodic movement is applied to the sample, and the second method with an extraction magnetometer in which the sample is subjected to a monotonic movement. Susceptibility of the sample has been determined by a graphical method (method of secants). It is worth pointing out that the non-deformed material has already susceptibility different from zero.

The results of measurements of magnetic susceptibility (permeability) converted to volume fraction of martensite versus plastic strain are indicated in Figure 5.4.

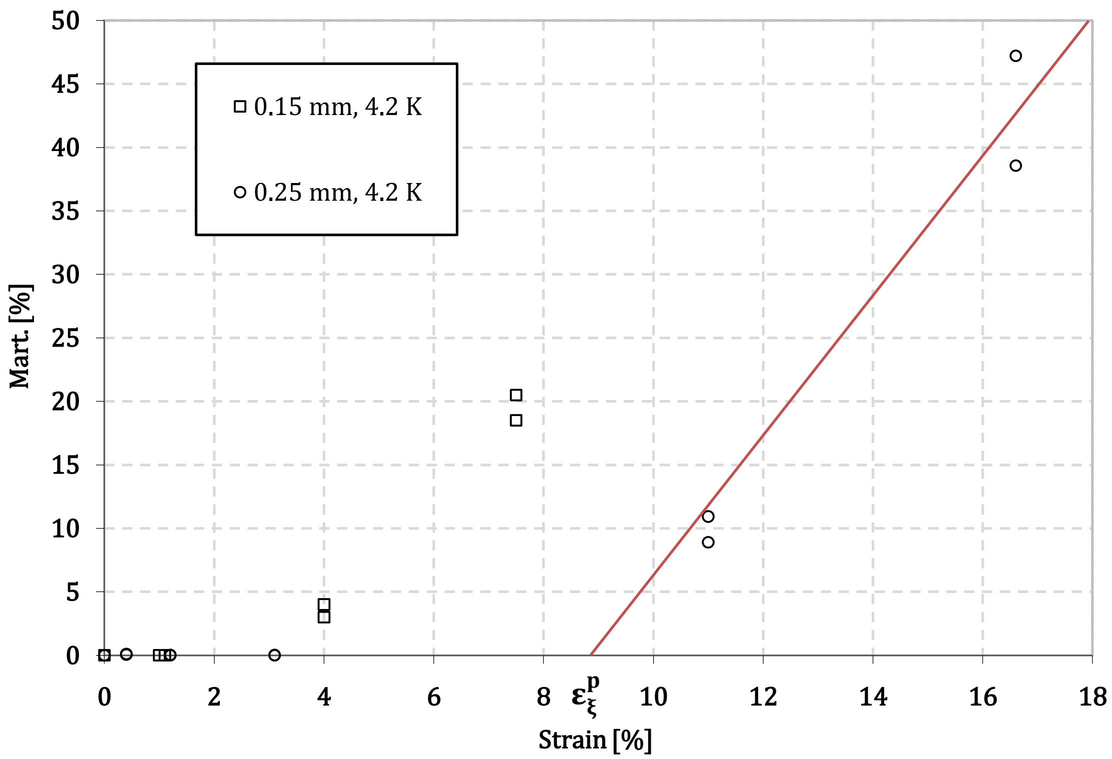

Figure 5.4 Martensite content as a function of strain at 4.2 K (0.15 mm, 0.25 mm)

The parameters of the kinetic law of phase transformation have been identified by using the above plotted data (0.25 mm, 4.2 K). The inelastic strain has been decomposed into plastic strain ε^{p} and the bain strain ε^{bs} according to the relationship:

$$\underline{\underline{\varepsilon}}^{inel} = \underline{\underline{\varepsilon}}^{p} + \xi \underline{\underline{\varepsilon}}^{bs} \tag{5.8}$$

Linearization of region II of the sigmoid curve has been carried out by using the least square method. The slope of the line and the intersection with the p-axis correspond to the function A and the threshold ε_{ξ}^{p}, respectively. As an example, identification of the parameters for grade 316L stainless steel at 4.2 K is shown in Figure 5.4.

5.3 Evolution of micro-damage

The damage variable, as introduced by Kachanov [42], has been defined on the basis of the irreversible thermodynamic processes leading to nucleation and growth of the micro-voids and micro-cracks in the entire volume of a sample. Here all types of voids and cracks (inter- and trans-granular) that spoil integrity of the material are accounted for. Thus, the process of damage development leads by definition to an increase of entropy [25].

The damage parameter, as defined by Eq. 2.2, is a non-negative state variable satisfying the following inequality:

$$0 \leq D \leq D_{cr} \tag{5.9}$$

where $D = 0$ for a non-damaged material and $D = D_{cr}$ for a decohesion of the sample (usually $D_{cr} \leq 1$, Fig. 5.3).

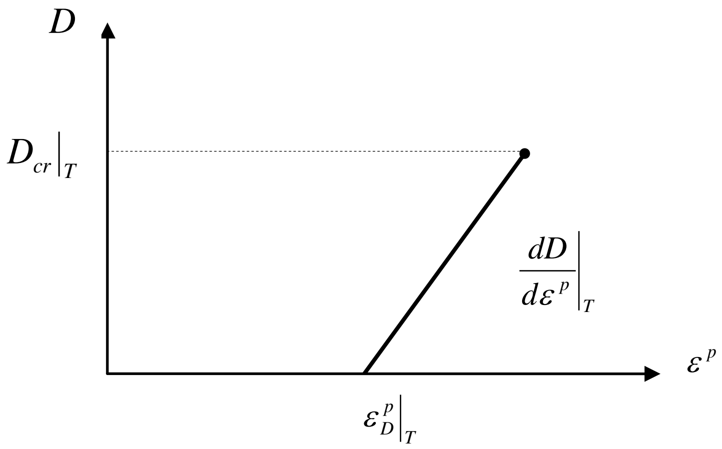

Figure 5.3 Linearized evolution of damage at a given temperature T: $\varepsilon_D^p\big|_T$ denotes damage threshold [25]

Since the damage evolution is a "dissipative" phenomenon, similar to the evolution of the plastic strain fields, a similar formulation for the potential of dissipation is applied (a continuous, convex scalar function of the dual variables):

$$\dot{D} = \frac{\partial F}{\partial Y}\dot{\lambda} \;\; ; \;\; F = \frac{S}{(s+1)(1-D)}\left(\frac{Y}{S}\right)^{s+1} \tag{5.10}$$

where S represents the strength energy of damage (material parameter) and s has to be identified by using the experimental data. Y denotes the strain energy density release rate expressed by:

$$Y = \frac{1}{2}\underline{\underline{\underline{\underline{K}}}}\,\underline{\underline{\varepsilon^e}}\,\underline{\underline{\varepsilon^e}} \tag{5.11}$$

Such a formulation yields the following kinetic law of damage evolution [43]:

$$\dot{D} = \left(\frac{Y}{S}\right)^{S} \dot{\varepsilon}^p H\left(\varepsilon^p - \varepsilon_D^p\right) \tag{5.12}$$

where ε_D^p is the so-called damage threshold.

The identification process has been carried out w.r.t. the experimental data from sample 7 of OFE copper. By means of unload-upload hysteresis loops the information about Young's modulus changes, appearing in the material during tension, was collected. The identified Young's moduli as well as the values of strain and stress for each hysteresis loop are presented in Table 5.2.

	ε [-]	σ [MPa]	E [GPa] - value between extreme points	E [GPa] - mean value on straight section
Test 1	0,0000	0		120
	0,0360	406	136,6	115
	0,0700	438	120,7	100
	0,1058	457	106,2	95
	0,1454	469	100,1	85
	0,1931	475	96,2	80
Test 2	0,2256	475	91,3	85
	0,2532	477	79,8	75
	0,2931	481	74,1	70
	0,3399	485	67,0	65
	0,3827	486	72,7	70
Test 3	0,4156	486	57,0	50
	0,4382	490	63,3	60

Table 5.2 Identification of Young modulus

Graphical representation of the Young modulus evolution is presented in Figure 5.4. The values of the Young modulus can be easily converted into damage parameter by using the following equation:

$$D = 1 - \frac{E}{E_0} \tag{5.13}$$

where E_0 is the Young modulus initial value and E refers to the values identified during successive unload-upload steps (Fig. 5.5).

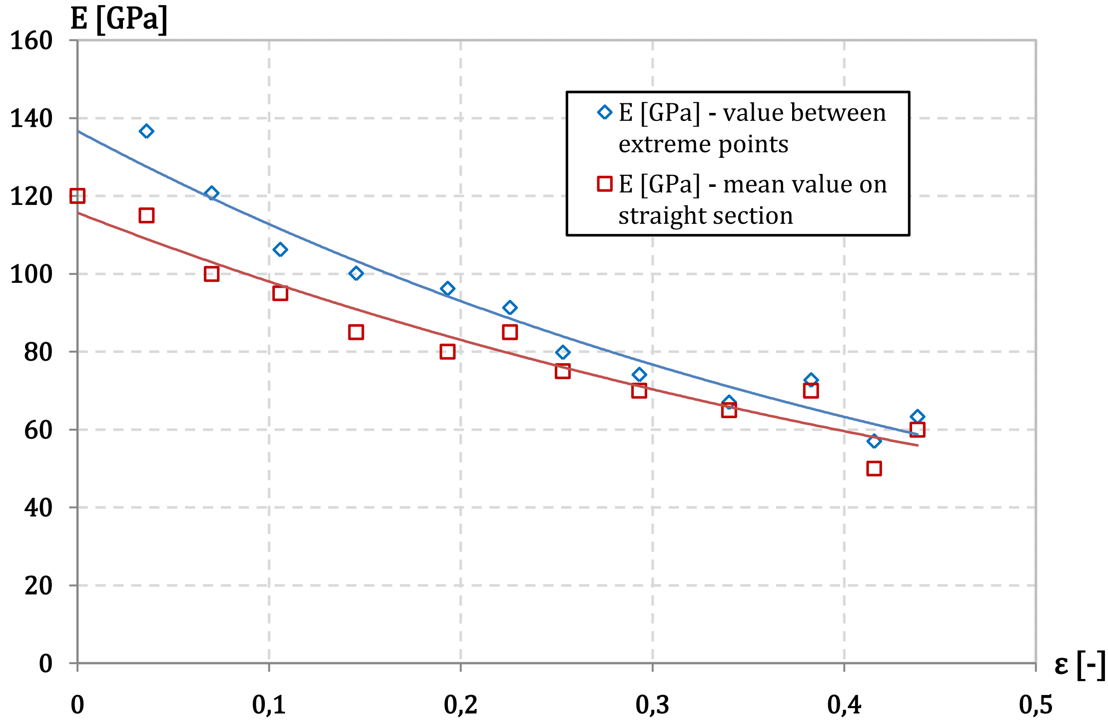

Figure 5.4 The Young modulus evolution for OFE Copper

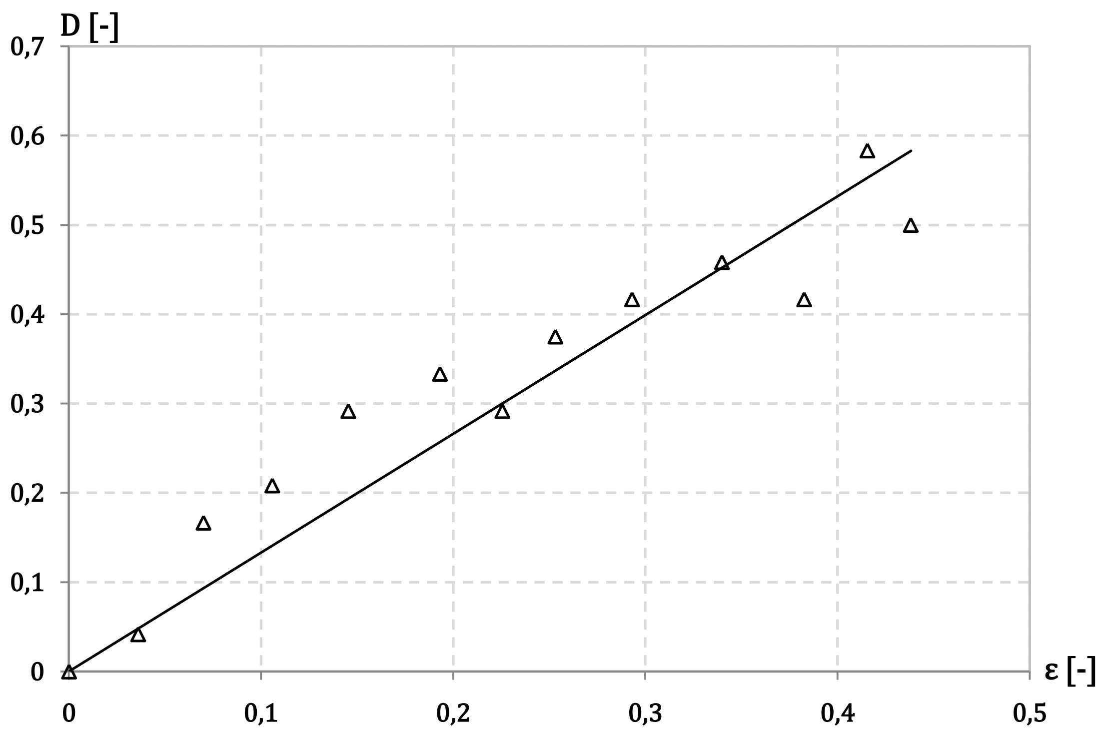

Figure 5.5 Identification of Damage parameter for OFE Copper

Chapter 6

Discussion of the results and conclusions

The low temperature behaviour of ductile materials is of great importance for construction of cryogenic systems. The main task of the Thesis consists in presenting experimental results of low temperature tests, focused on specific phenomena that occur at cryogenic temperatures. Apart from discontinues plastic flow and evolution of micro-damage the phenomenon of plastic strain induced γ-α' phase transformation has been analysed in order to show all three complementary effects. Another aspect consists in presenting complex experimental set-up, constructed at CERN in order to test materials applied at low temperatures.

The unique experimental set-up consists of tensile testing machine, cryostat with all necessary instrumentation (sensors) and the data acquisition system that was upgraded to achieve the possibility of recording experimental data with uncommon frequency of 20 kHz. Moreover, the internal force cell was mounted just next to the specimen inside the cryostat. As a result, the obtained experimental data were more precise than any other data obtained in the past.

The experimental results obtained during testing summed up to a rather impressive collection of data related to cryogenic phenomena. The most important results are certainly high frequency records of serrated yielding observed on four types of materials: pure copper, two copper-zirconium alloys and stainless steel 316 LN. The comparison of stress-strain curves showed significant differences in the phenomenon appearance, especially between copper and stainless steel. Besides that, the representation of stress, strain and temperature as a function of time allows to investigate serrations with a precision down to some 0,05 ms. The second important result was the examination of the range of discontinues plastic flow in terms of the strain rate. It is shown that the upper limit of this range is related to rising temperature due to fast plastic deformation of the sample.

The study of Young's modulus evolution along the specimen deformation is worth mentioning. The examination was made by means of the unloading parts of stress-strain curves for the engineering stress-strain values.

This study has provided useful information about some of the cryogenic phenomena that should be taken into account during the design of low temperature systems. It has also shown how important a research of undesirable low temperature effects might be to predict their influence on the mechanical objects designed for cryogenic conditions.

Bibliography

1. **CERN Webpage.** 2009. *Home > About us.* [Online] CERN, http://public.web.cern.ch/public/en/About/About-en.html.
2. **CERN Document Server Webpage.** 2009. *Home > Multimedia & Outreach > Photos.* [Online] CERN, http://cdsweb.cern.ch/collection/Photos?ln=en.
3. **CERN Webpage.** 2009. *Home > The LHC > Facts and figures > CERN FAQ – LHC the guide.* [Online] CERN, http://cdsweb.cern.ch/record/1165534/files/CERN-Brochure-2009-003-Eng.pdf.
4. **Lebrum, P.** 2003. *Cryogenics, Key to Advanced Science and Technology.* Bulletin of the IIR.
5. **Basiński, Z. S.** 1957. *The Instability of Plastic Flow of Metals at Very Low Temperatures.* Proceedings of the Royal Society, Ser. A, 240, pp. 229-242.
6. **Dolgin, A. M. and Natsik, V.D.** 1991. *Criteria of Instabilitie and Kinetics of Jumps Under Unstable Low Temperature Plastic Flow.* Acta Universitatis Carolinae - Mathematica et Physica, vol. 32, 1, pp. 77-88.
7. **Basiński, Z. S.** 1960. *The Instability of Plastic Flow of Metals at Very Low Temperatures II.* Australian Journal of Physics, vol. 13, p. 354.
8. **Shibata, K.** 1989. *Discussion about Basinski's Model for Serration at Very Low Temperature with Computer.* Cryogenic Materials '88 - Structural Materials, vol. 2, pp. 865-872.
9. **Seeger, A.** 1957. [red.] Fischer, J. C., Johnston, W. G., Thomson, R. and Vreeland, T. Jr. *Dislocations and Mechanical Properties of Crystals.* New York : Wiley.
10. **Trefilov, V. I., Milman, Yu. V. and Firstov, S. A.** 1975. *Phyzicheskie Osnovi Prochnosti Tugoplavkih Metallov.* Naukova Dumka, p. 315.

11. **Prioul, C., Rodrigues, C. A. and Libeyre, P.** 1986. *Tensile and Fatigue Properties of 316LN Austenitic Steel at Cryogenic Temperatures.* Fusion Technology 1986 - Proceeding of 14th Symposium, vol. 2, pp. 1051-1055.

12. **Reed, R. P., Simon, N. J., Purtscher, P. T. and Tobler, R. L.** 1986. *Alloys 316LN for Low Temperature Structures: A Summary of Tensile and Fracture Data.* 11th International Cryogenic Engineering Conference.

13. **Ogata, T., Umezawa, O. and Ishikawa, K.** 1990. *Low Temperature Creep Behavior of Stainless Steel.* Advence in Cryogenic Engineering Materials, vol. 36, pp. 1233-1239.

14. **Ogata, T., Ishikawa, K., Nagai, K., Umezawa, O. and Yuri, T.** 1990. *Low Cycle Fatigue and Other Mechanical Properties of Aged 316LN Stainless Steel at Liquid Helium Temperature.* Advence in Cryogenic Engineering Materials, vol. 36, pp. 1249-1255.

15. **Obst, B. and Nyilas, A.** 1991. *Experimental Evidence on the Dislocation Mechanism of Serrated Yielding in F.C.C. Metals and Alloys at Low Temperatures.* Materials Science and Engineering, A, 137, pp. 141-150.

16. **Obst, B. and Nyilas, A.** 1998. *Time-resolved Flow Stress Behavior of Structural Materials at Low Temperatures.* Advances in Cryogenic Engineering, vol. 44, pp. 331-337.

17. **Berrahmoune, M. R., Berveiller, S., Inal, K., Moulin, A. and Patoor, E.** 2004. *Analysis of the Martensitic Transformation at Various Scales in TRIP Steel.* Materials Science and Engineering, A, 378, pp. 304-307.

18. **Purtschar, P. T., Walsh, R. P. and Reed, R. P.** 1988. *Effects of Chemical Composition on the 4K. Mechanical Properties of 316LN-type Alloys.* Advances in Cryogenic Engineering Materials, vol. 34, pp. 191-198.

19. **Purtschar, P. T., Walsh, R. P. and Reed, R. P.** 1988. *Fracture Behaviour of 316LN Alloy in Uniaxial Tension at Cryogenic Temperatures.* Advances in Cryogenic Engineering Materials, vol. 34, pp. 379-386.

20. **Reed, R. P. and Walsh, R. P.** 1988. *Tensile Strain-rate Effects in Liquid Helium.* Advance in Cryogenic Engineering Materials, vol. 34, pp. 199-208.

21. **Estrin, Y. and Tangri, K.** 1981. *Thermal Mechanism of the Anomalous Temperature Dependence of the Flow Stress.* Scripta Metallurgica, vol. 15, pp. 1323-1328.

22. **Garion, C. and Skoczeń, B.** 2002. *Modelling of Plastic Strain-induced Martensitic Transformation for Cryogenic Applications.* Journal of Applied Mechanics, vol. 69, 6, pp. 755-762.

23. **Morris, J. W., Chan, J. W. and Mei, Z.** 1992. *The Influence of Deformation-induced Martensite on the Crygenic Behavior of 300-series Stainless Steels.* Cryogenics 1992 - ICCM supplement, vol. 32.

24. **Suzuki, K., Fukakura, J. and Kashiwaya, H.** 1988. *Cryogenic Fatigue Properties of 304L and 316L Stainless Steels Compared to the Mechanical Strength and Increasing Magnetic Permeability.* Journal of Testing and Evaluation, vol. 16, 2.

25. **Garion, C. and Skoczeń, B.** 2002. *Plastic Strain Induced Damage Evolution and Martensitic Transformation in Ductile Materials at Cryogenic Temperatures.* Advences in Cryogenic Engineering, vol. 48, pp. 170-177.

26. **Moulis, S.** 2005. *Optimisation de la Ligne d'Essais Mécaniques à Température Cryogénique (4.2 K) par Introduction d'un Capteur à Jauges de Contrainte.* Geneva : CERN.

27. **Bonhomme, S.** 2003. *Modernisation des Essais de Traction à Basse Température et Mesure de l'Effet de Serration.* Geneva : CERN.

28. **Aziri, D.** 2001. *Caractérisation à 4.2 K des Soufflets en 316L pour les Interconnexions du LHC.* Geneva : CERN.

29. **LakeShore Webpage.** 2009. *Home > Temperature Sensors > Cernox.* [Online] Lake Shore Cryotronics, http://www.lakeshore.com/temp/sen/crtd.html.

30. **Sensorex Webpage.** 2009. *Home > Support > Directory.* [Online] Sensorex, http://www.sensorex.fr/en/articles/articles.php4?_id=3&titre=Support.

31. **Thames-Side Webpage.** 2002. *Series U2000 Miniature Tension/Compression Load Cell for Force Measuring.* [Online] Thames-Side, http://www.thames-side.com/pdf/u2000.pdf.

32. **Portier, N.** 2004. *Essais Mécaniques à Basse Température: Optimisation de la Chaîne d'Acquisition pour Permettre un échantillonnage à très haute Fréquence.* Geneva : CERN.

33. **Grout, A.-L.** 2007. *Test de Traction à 4.2 K.* Geneva : CERN.

34. **NI Webpage.** 2009. *Home > Products & Services > Data Acquisition.* [Online] National Instruments Corporation, http://sine.ni.com/nips/cds/view/p/lang/en/nid/11913.

35. **Davis, J. R. [red.]** 2001. *ASM Specialty Handbook: Copper and Copper Alloys.* Ohio : ASM International.

36. **Reed, R. P.** 1983. *Materials at Low Temperatures.* Ohio : ASM International.

37. **Skoczeń, B., Bielski, J., Sgobba, S. and Marcinek, D.** 2009. *Constitutive Model of Discontinuous Plastic Flow at Cryogenic Temperatures.* International Journal of Plasticity.

38. **Olson, G. B. and Cohen, M.** 1975. *Kinetics of Strain-induced Martensitic Nucleation.* Metallurgical Transactions, 6A, pp. 791-795.

39. **Stringfellow, R. G., Parks, D. M. and Olson, G. B.** 1992. *A Constitutive Model for Transformation Plasticity Accompanying Strain-induced Martensitic Transformations in Metastable Austenitic Steels.* Acta Metallurgica et Materialia, vol. 40, 7, pp. 1703-1716.

40. **Levitas, V. I., Idesman, A. V. and Olson, G. B.** 1998. *Continuum Modeling of Strain-induced Martensitic Transformation at Shear-band Intersections.* Acta Materialia, vol. 47, 1, pp. 219-233.

41. **Garion, C., Skoczen, B. and Sgobba, S.** 2006. *Constitutive Modelling and Identification of Parameters of the Plastic Strain-induced Martensitic Transformation in 316L Stainless Steel at Cryogenic Temperatures.* International Journal of Plasticity, vol. 22, 7, pp. 1234–1264.

42. **Kachanov, L. M.** 1986. *Introduction to Continuum Damage Mechanics.* Dordrecht : Martinus Nijhoff.

43. **Lemaitre, J.** 1992. *A Course on Damage Mechanics.* Berlin : Springer.

Appendices

A Temperature sensor – certificate of calibration

CERTIFICATE OF CALIBRATION

Calibration Report: 268407 Sensor Serial Number: X04360

Sensor Type: Cernox Resistor Model: CX-1050-SD

This temperature sensor has been calibrated against standards maintained by Lake Shore Cryotronics, Inc.

All calibrations provided by Lake Shore are based on the International Temperature Scale of 1990 (ITS-90) above 0.65K. At lower temperatures (below 0.65K), a cerium magnesium nitrate magnetic thermometer has been used in conjunction with National Institute of Standards and Technology superconducting fixed points Standard Reference Material 768 to generate a scale.

Each scale is currently maintained on a set of germanium or platinum resistance standards, as appropriate, which are routinely checked by intercomparison and periodically calibrated by the United States National Institute of Standards and Technology or Great Britain's National Physical Laboratory.

Lake Shore's calibration facility and procedures for diode and resistance sensor calibrations above 1.2K are maintained traceable in accordance with MIL STD 45662A.

Date: March 19, 1996

Recommended Recalibration Date: March 19, 1997

Reported By: Approved By:

LakeShore
Measurement and Control Technologies

Lake Shore Cryotronics, Inc.
64 East Walnut Street ● Westerville, Ohio 43081-2399
Fax: (614) 891-1392 ● E-mail: sales@lakeshore.com
Tel: (614) 891-2243

POLYNOMIAL EQUATION
Calibration Report: 268407
Sensor Type: Cernox Resistor

Sensor Serial Number: X04360
Sensor Model: CX-1050-SD

Polynomial Type: Chebychev
Useful range of fit: 4.00 to 22.7 K

Lower and upper limits of Log(Resistance (Ω)) used in computing Chebychev coefficients:

ZL = 2.68443797730 ZU = 3.74804059424

Order	Coefficient	Std. Dev. of Coeff.	Ratio (Coeff./Std. Dev.)
0	11.362985	2.0202D-04	56245.94
1	-10.382328	3.1000D-04	-33491.57
2	3.261426	3.0393D-04	10730.73
3	-.760696	2.8582D-04	-2661.49
4	.125524	2.7507D-04	456.33
5	-.011296	2.6284D-04	-42.98
6	.000127	2.5484D-04	.50

Z = Log(Resistance)

X = ((Z-ZL)-(ZU-Z))/(ZU-ZL)

Temp. (K) = Σ A_i * COS(i * ARCCOS(X)),
where 0 <= i <= 6 and the A_i's are the coefficients
in the table above.

POLYNOMIAL EQUATION
Calibration Report: 268407
Sensor Type: Cernox Resistor

Sensor Serial Number: X04360
Sensor Model: CX-1050-SD

Polynomial Type: Chebychev
Useful range of fit: 22.7 to 100 K

Lower and upper limits of Log(Resistance (Ω)) used in computing Chebychev coefficients:

ZL = 2.05614408244 ZU = 2.79327749892

Order	Coefficient	Std. Dev. of Coeff.	Ratio (Coeff./Std. Dev.)
0	59.020545	1.2731D-03	46360.97
1	-48.328391	2.0615D-03	-23443.64
2	10.881324	1.8944D-03	5743.85
3	-1.663639	1.7355D-03	-958.61
4	.176966	1.6349D-03	108.24
5	-.004189	1.6284D-03	-2.57
6	-.000515	1.5940D-03	-.32

Z = Log(Resistance)

X = ((Z-ZL)-(ZU-Z))/(ZU-ZL)

Temp. (K) = Σ A_i * COS(i * ARCCOS(X)),
where 0 <= i <= 6 and the A_i's are the coefficients
in the table above.

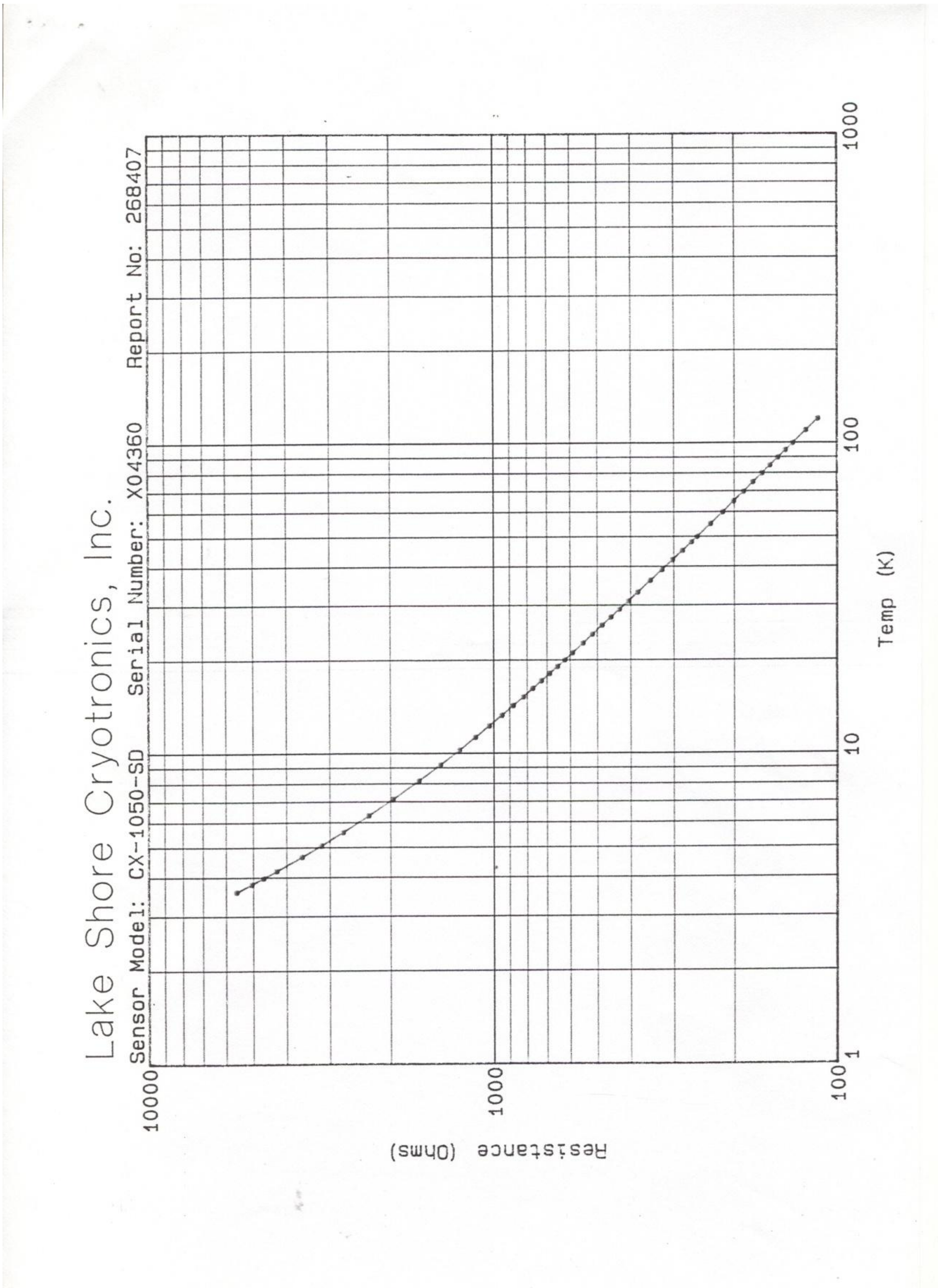
Lake Shore Cryotronics, Inc.
Sensor Model: CX-1050-SD
Serial Number: X04360
Report No: 268407
Temp (K)
1
10
100
1000
Resistance (Ohms)
10000
1000
100

B LVDT – certificate of calibration

Sensorex

SG 144 C01

CAPTEUR DE DEPLACEMENT A TRANSFORMATEUR DIFFERENTIEL / RELEVE DE MESURES

LINEAR VARIABLE DIFFERENTIAL TRANSFORMER TEST AND INSPECTION DATA

NUMERO DE SERIE/*SERIAL NUMBER* : 1754 *DATE* : 12-12-02

☒SX 9 W3........ ☐SX 12K........ ☐Option P (250 bar) ☐Option HP (350 bar) ☐Option HT (200°C)

....

A LIRE AVANT UTILISATION DU CAPTEUR

Ce capteur de mesure est fabriqué avec des moyens de haute technologie. Il est soigneusement contrôlé dans nos locaux et fonctionne correctement lors de son expédition.
Afin d'obtenir les meilleures performances, manipuler l'appareil avec soin lors de son installation.
Ne pas usiner, écraser ou percer l'équipage mobile ou le capteur.
L'équipage mobile et le capteur sont appairés, de ce fait et pour de meilleures performances, il est recommandé de ne pas les dissocier.

PLEASE READ BEFORE USING THE TRANSDUCER

This measurement device is manufactured to high precision standards.
Our factory checks its performance prior to shipment. To obtain the optimum performance in your applications, handle and install with care.
Do not machine, grind or drill core and coil assembly. Core and coils are matched sets, for best performance do not interchange cores.

CARACTERISTIQUES / SPECIFICATIONS

Excitation primaire	/ *Input voltage*	: 2,2 Veff/rms
Fréquence	/ *Frequency*	: 3500 Hz
Course	/ *Stroke*	: ± ...1,5... mm
Sensibilité	/ *Sensitivity*	: ...144,81... mV/Vmm
Phase primaire secondaire	/ *Prim. second. phase*	: OK ☒
Dérive en température	/ *Temperature drift*	: < 150 < ~~300~~ < ~~350~~ < ~~500~~ ppm/°C
Linéarity	/ *Linearity*	: ± 0,10 ± ~~0,15~~ ± ~~0,25~~ ± ~~0,30~~ % pleine échelle (of full scale output)
Charge secondaire	/ *Secondary load*	: 100 Kohm

SX 9 W3

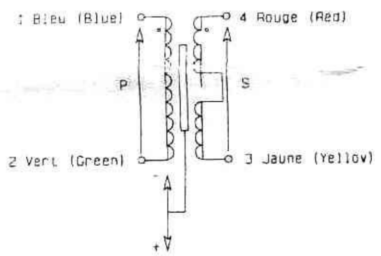

SX 12 K

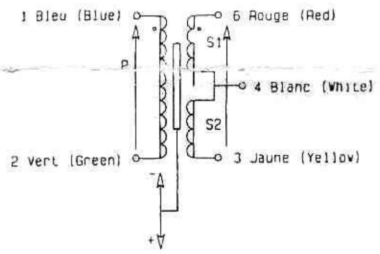

CONTRÔLE QUALITÉ

Visa Contrôle Qualité/Quality Control Visa

DEC. 2002

SENSOREX

SENSOREX
Parc d'Affaires International – Archamps
74166 St Julien en Genevois Cedex
Tél : 04-50-95-43-55
Fax : 04-50-95-43-75

Sensorex SA

Code Produit................ standard
(LVDT Reference)
Désignation LVDT..... SX 9 W 3
(LVDT Name)
Numéro de Série.......... 1754
(Serial Number)

Rapport De Controle Final
(Acceptance Test Report)

N	course stroke (mm)	mesure (R.cos)	phase (deg)	Erreur de Lin (%PE)
1	-1.50	-0.2992	187.8	0.10
2	-1.17	-0.2330	187.6	0.06
3	-0.84	-0.1666	187.4	0.00
4	-0.51	-0.1008	187.1	-0.03
5	-0.18	-0.0342	186.3	0.03
6	0.16	0.0316	8.6	-0.08
7	0.48	0.0965	7.9	-0.10
8	0.81	0.1618	7.8	-0.07
9	1.14	0.2292	7.8	-0.02
10	1.48	0.2966	7.9	0.10

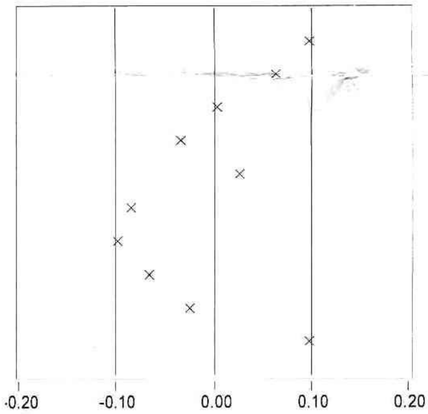

------CONDITIONS DE MESURE-----
(TEST CONDITIONS)

Fréquence Générateur... 3500 Hertz
(Generator Frequency)

Tension Primaire............ 2.20 V rms
(Input Voltage)

Charge Secondaire......... 100k
(Secondary Load)

Meilleur Droite
(Best Fit Line)

------------------RESULTATS------------------
(RESULTS)

Sensibilité Calculée.......... 199.81 mV/(V.mm)
(Sensitivity Computed)

Résiduelle........................... 0.0 mV rms
(Null Voltage)

Erreur Max de Linéarité... +/- 0.10 %
(Maximum Linéarity Error)

Banc de Test n°3
(Test System n°3)

Form. SG445A mar. 10 déc. 2002

CONTRÔLE QUALITÉ
12 DEC 2002
SENSOREX

C External load cell – certificate of calibration

Certificate of Calibration

Unit Type » T220N253(U2000) Serial Number » 0228942

Unit Range » 25000N Date » 16/02/2004

CALIBRATION

Input Resistance » 755 Ohms Output Resistance » 707 Ohms

Recommended Excitation » 10 Volts

Maximum Excitation » 15Volts

Sensitivity » 1.76562 mV/V

Combined Error (Non-Linearity and Hysteresis) » < ± 0.1 % of F.S

Compensated Temperature Range » -0 °C to +60°C

Operable Temperature Range » -40 °C to +80°C

Thermal Zero Shift » ± 0.02 % of F.S./°C

Thermal Span Shift » ± 0.005 % of F.S./°C

Data obtained utilising standards traceable to NAMAS Force Calibration Laboratory.

WIRING

+ Excitation	RED
- Excitation	BLUE
+ Output	GREEN
- Output	YELLOW

signed:-

Department:- Quality Assurance

D Specifications of the NI 6036E PCI card

This appendix lists the specifications of the NI 6034E/6035E/6036E device. These specifications are typical at 25 °C unless otherwise noted.

Analog Input

Input Characteristics

Number of channels .... 16 single-ended or 8 differential (software-selectable per channel)

Type of ADC... Successive approximation

Resolution .... 16 bits, 1 in 65,536

Sampling rate .... 200 kS/s guaranteed

Input signal ranges .... Bipolar only

Device Gain (Software-Selectable)	Range
0.5	±10 V
1	±5 V
10	±500 mV
100	±50 mV

Input coupling .... DC

Overvoltage protection

Signal Name	Powered Off
ACH<0..15>	±15 V
AISENSE	±15 V

E Technical specification of copper bar

CERN

Materials Technical Specification (FI-LS)

TECHNICAL SPECIFICATION

N° 2001 - Ed. 7 - 11.10.2006

BAR

COPPER OFE

Original: English

CONTENTS

../...

COPPER OFE

---

1. ***GENERAL***

APPLICATIONS

This specification relates to copper OFE (ASTM B224-04, Oxygen-free, electronic; ASTM B170-99(2004), Grade 1, UNS C10100; ISO 431, Cu-OFE) for bar fabrication.

Some sizes are standard stock in CERN stores and have an internal SCEM reference.

2. ***APPLICABLE DOCUMENTS***

Reference is made in this specification to the documents below:

ISO 431	(1981)	Copper refinery shapes
ASTM B224-04	(2004)	Standard classification of coppers
ASTM F68-05	(2005)	Standard Specification for Oxygen-Free Copper in Wrought Forms for Electron Devices
ASTM E112-96(2004)e1	(2004)	Standard method for determining average grain size
ASTM B170-99(2004)	(2004)	Standard specification for oxygen-free electrolytic copper - refinery shapes
ASTM B193-02	(2002)	Standard test method for resistivity of electrical conductor materials
MIL-STD-2154	(1982)	Inspection, ultrasonic, wrought metals, process for
prEN 4050-4:1994		Aerospace series - Test method for metallic materials; ultrasonic inspection of bars, plates, forging stock and forgings - Part 4: Acceptance criteria

../...

BAR 4

COPPER OFE

---

3. ***GENERAL CHARACTERISTICS***

3.1 CHEMICAL COMPOSITION

The reference publications are standards ASTM F68-05, B170-99(2004) and ISO 431.
Cu min: 99.99%

The impurities shall be in accordance with ISO 431 except:

O_2	5 ppm max.

Impurities:

Element		Cu-OFE
Copper	min.	99.99
Cadmium	max.	0.0001
Phosphorus	max.	0.0003
Sulphur	max.	0.0018
Zinc	max.	0.0001
Mercury	max.	0.0001
Lead	max.	0.001
Selenium	max.	0.001
Tellurium	max.	0.001
Bismuth	max.	0.001
Arsenic Antimony Bismuth Selenium Tellurium Tin Manganese		Total of these seven elements not to exceed 40 ppm

3.2 PROPERTIES

3.2.1 Structure

In accordance with the standard ASTM E112-96(2004)e1, grain size ≤ 90 µm shall be accepted.

For certain applications the grain size may be the subject of a specific discussion between CERN and the manufacturer.

../...

3.2.2 Inclusions

In accordance with standard ASTM F68-05, only Classes 1 and 2 shall be accepted.

3.2.3 Mechanical

Tensile testing must be performed on test samples with their longitudinal axis parallel to that of the bars.

At room temperature:

Tensile strength	R_m		240 - 280 N/mm^2
Yield stress	R_p 0.2%		200 - 240 N/mm^2
Elongation at break	A_5	min.	25%

3.2.4 Electrical (as per ASTM B193)

Conductivity in the annealed condition min. 101% IACS

3.2.5 Guaranteed thermal conductivity

Conductivity at 4.2 K 400 $Wm^{-1}K^{-1}$

4. *MANUFACTURING PROCESS*

In accordance with the diameter, the bars shall be given the necessary treatment to allow delivery in the **HALF-HARD** state.

5. *QUALITY CONTROL*

5.1 GENERAL

Quality control shall be carried out in accordance with a Quality Control Plan (QCP) established between the manufacturer and CERN. CERN (or its representative) reserves the right to intervene during the different stages of fabrication.

5.2 HOMOGENEITY

The homogeneity of the bar shall be ultrasonically inspected solely to detect continuity faults. Each copper bar shall be ultrasonically tested at frequencies ≥ 4 MHz, depending on the thickness.

Acceptance criteria for the bars, inspected 100 % in accordance to MIL-STD 2154:1982 or equivalent, and accepted according to prEN 4050-4:1994, are following class 3 or higher of prEN 4050-4:1994. A class higher than 3 will be imposed by CERN in some cases, depending on the thickness of the product and the final application.

The FBH reference shall be set according to the relevant class. Reject when:

1) Ultrasonic indications greater than the value given in Table 1 of prEN4050-4:1994.

2) Loss in back wall echo greater than 20% screen height.

Ultrasonic testing shall be performed in accordance with a written procedure that shall be submitted to CERN for approval prior to testing.

5.3 QUALIFICATION CONTROL (to the standards in force)

For each batch or copper bar delivered, the following tests shall be carried out by the manufacturer on each item delivered:

- Metallography
- Chemical analysis
- Mechanical properties
- Electrical properties
- Hydrogen embrittlement
- Ultrasonic examination (see § 5.2)
- Dimensional check (see § 1)

5.4 IDENTIFICATION

Each bar shall be marked with :

- batch number (cast number)
- supplier's name
- type of material

The markings shall be mechanically engraved at each end.

5.5 DOCUMENTS

The supplier shall attach the analysis certificates issued following the qualification controls given in § 5.3 above to each consignment.

All these certificates shall be drawn up in accordance with the prevailing standards.

6. *PACKING*

The material is to be delivered as packed in the factory.

The packing material used shall be sufficiently robust to ensure that the surface is maintained in good condition during transport.

../...